

The Projection Spectral Layer Theory (PSLT): A Rank-2 Computable Closure for the Three-Generation Structure and Higgs Signal Strength

Bo-Yu Chen¹

¹*Independent Researcher*

(Dated: February 2, 2026)

We present a comprehensive, computable EFT-level “closed chain” for the Projection Spectral Layer Theory (PSLT) that naturally generates a self-consistent three-generation structure of matter. The framework is built on a minimal Einstein–Yang–Mills–Higgs (EYMH) effective action with non-minimal curvature coupling, where the background geometry induces a layer-indexed spectral scale ω_N . The theoretical closure is achieved by unifying three key modules: (i) a **Micro-degeneracy module** (g_N) modeled by a Cardy-controlled envelope with an explicit high- N regulator ($q^{(N-1)^2}$ -type suppression) that prevents entropic runaway; (ii) a **Rank-2 Computable Kinetic module** (Γ_N) defined as the largest positive eigenvalue of a 2×2 growth matrix with explicit WKB tunneling suppression; and (iii) a **Visibility module** (B_N) anchored to Standard Model lepton Yukawa couplings via a sublinear compression exponent $0 < p_B < 1$, with high- N saturation ($B_{N>3} = 1$) to avoid double-counting with the g_N regulator. The resulting normalized layer probability $P_N(t_{\text{coh}})$ demonstrates a stable “winner” phase diagram with clear dominance of layers $N = 1, 2, 3$ over a significant region of the geometric parameter space (D, η) . We verify the closure against two benchmarks: (1) internal stability of the three-generation hierarchy (Generation Ratio $> 90\%$ over 80.0% of the sampled (D, η) grid), and (2) a proxy compatibility test with the ATLAS Run-3 $H \rightarrow \mu\mu$ signal strength ($\mu_{\mu\mu}^{\text{obs}} = 1.4 \pm 0.4$). The proxy mapping yields a restricted acceptance band (about 9.4% of the scanned grid for $\chi^2 < 4$), providing a sharper falsifiable constraint on (D, η) .

CONTENTS

I. Introduction	4
II. Theoretical Framework	5
A. The Closed Chain Equation	5
B. Action-Derived Chain at a Glance	5
C. Geometric Foundation: Minimal EYMH + Curvature	5

D. Model-Chain Assumption Status	7
III. Geometry-to-Spectrum Worked Example	8
A. Two-Center Harmonic Conformal Factor	9
B. Action-Derived Effective Potential	9
C. Numerical Solution	10
D. Single-Track Results	10
E. Summary: Unified Geometry-to-Kinetics Pipeline	10
IV. Module 1: The Three Routes to Micro-Degeneracy gN	13
A. Route A: Mock-Modular Counting	13
B. Route B: ER=EPR and Entanglement Entropy	13
C. Route C: Quantum Gravity Template	13
D. Unified Cardy-Controlled Envelope with High-N Regulator	13
E. Cardy Regime Validity and Finite-N Corrections	14
F. Assessment of a Phase-Space First-Principles Candidate	15
V. Module 2: Rank-2 Computable Kinetics GammaN	15
A. Dual-Center Tunneling Suppression	15
B. Dimensionality and Units	16
C. Derivation of the Rank-2 Growth Matrix	16
D. Rank-2 Computable Closure	16
E. Physical Interpretation: Quasi-Bound State Decay	17
VI. Module 3: Yukawa-Anchored Visibility BN	18
A. High- N Saturation (Avoiding Double-Counting)	20
B. Roadmap: Action-Derived Effective Yukawa Operator	20
VII. Verification Results	20
A. Configuration and Parameter Table	20
B. Three-Generation Phase Diagram	21
C. H to mu mu Signal Strength (Observable Proxy)	22
D. Proxy Extension to H to ee and H to tau tau	23
VIII. Discussion and Conclusion	24
Acknowledgments	26

A. Action-Derived Chain Reproducibility SOP	26
1. Single Entry Point	26
2. Step Map and Deliverables	26
3. Acceptance Conditions	26
B. Action-Derived Effective Potential and WKB	27
1. Two-Center Harmonic Conformal Factor	27
2. V_{eff} Derivation from KG Equation	28
3. 1D On-Axis Reduction	29
4. 2D Axisymmetric Validation	29
5. WKB Action Convention	29
6. Splitting–Action Consistency Check	30
7. Action-Derived Numerical Results	30
8. Bound-State omega Convergence Benchmark	31
9. Fixed-dz Convergence	31
C. First-Principles Symmetry-Channel Test for chi	32
D. Localized-Channel First-Principles Extraction of chi	32
E. Preliminary First-Principles Replacement Candidate Checks	35
1. 1D Phase-Space Candidate for g_N	35
2. 2D Axisymmetric Benchmark for $g_N^{(\text{ps})}$	36
3. Geometry-Informed Lindblad Scan-Ready Module for Open-System χ	38
4. Cross-Module Migration Snapshot	39
5. Dephasing-Based First-Principles Candidate for t_{coh}	40
6. Splitting-Prefactor First-Principles Candidate for η	41
7. Action-Derived First-Principles Candidate for Superradiant Channel Scaling	42
F. Ansatz Ablation Study	44
1. Inverse Yukawa Ansatz (Ablation A)	44
2. Comparison	44
References	44

I. INTRODUCTION

The existence of exactly three generations of fermions is one of the most persistent puzzles in the Standard Model (SM) of particle physics. While the SM accommodates three families through the CKM and PMNS mixing matrices, it offers no dynamical reason for why the number is three, nor why the mass hierarchy spans such a vast range. Traditional attempts to explain this structure often rely on complex discrete symmetries or string logic compactifications that, while elegant, can be difficult to falsify directly.

The Projection Spectral Layer Theory (PSLT) proposes a different paradigm: *Generation structure is a spectral consequence of the underlying projection geometry of spacetime.* In this framework, "generations" are not ad-hoc copies but rather distinct *spectral layers* ($N = 1, 2, 3, \dots$) of vacuum excitations, selected by a competition between microstate degeneracy (entropy) and geometric formation rates (kinetics). This structural viewpoint is complementary to recent Clifford-algebra work where three families emerge from an intrinsic S_3 organization rather than manual generation copying [1]; the emphasis here is different: a map-level computable closure with explicit scan-level falsifiability.

In this work, we consolidate the complete theoretical framework of PSLT into a single, falsifiable "closed chain". We upgrade earlier effective descriptions to a **computable** rank-2 dynamical system with an action-derived extraction subchain and a surrogate global scan chain. The core deliverable is a map from geometric control parameters (D, η) —representing dual-center separation and overlap—to an experimentally observable layer probability P_N .

Our primary contributions are:

1. **Theoretical Motivation:** We present three convergent arguments for the microdegeneracy g_N (Route A: Mock-modular, Route B: ER=EPR, Route C: QG Template) as motivations for a Cardy-controlled envelope, and make the closure numerically stable by adding an explicit high- N regulator.
2. **Rank-2 Computable Kinetics:** We replace heuristic growth rates with a rigorous eigenvalue problem for the formation matrix \mathbf{M}_N , incorporating numerical WKB tunneling suppression.
3. **Yukawa-Anchored Visibility:** We anchor B_N to Standard Model lepton Yukawa couplings with a sublinear compression exponent, and use high- N saturation ($B_{N>3} = 1$) to avoid double-counting with the g_N regulator.
4. **Verification:** We demonstrate stable three-generation dominance at $\mathcal{R}_3 > 90\%$ and a

constrained proxy-compatible band for LHC $H \rightarrow \mu\mu$.

II. THEORETICAL FRAMEWORK

A. The Closed Chain Equation

The central output of the PSLT framework is the normalized layer occupancy probability $P_N(t_{\text{coh}})$, defined by the competition between entropic weight (W_{entropy}) and kinetic formation (W_{kinetic}). The master equation is:

$$P_N(t_{\text{coh}}; D, \eta) = \frac{W_N(t_{\text{coh}})}{\sum_K W_K(t_{\text{coh}})}, \quad W_N = B_N \cdot g_N \cdot \left(1 - e^{-\Gamma_N(D, \eta)t_{\text{coh}}}\right). \quad (1)$$

This equation unifies the three critical modules:

- g_N : **Micro-degeneracy** (Entropy). The number of available microstates in layer N .
- Γ_N : **Dynamical Rate** (Kinetics). The rate at which these states can form/tunnel from the vacuum.
- B_N : **Visibility Factor** (Observation). The coupling strength of layer N to the observable sector.

Figure 1 illustrates the logical flow of the PSLT framework.

B. Action-Derived Chain at a Glance

For implementation-level clarity, Figure 2 summarizes the action-derived operator chain and its interfaces to scan-level diagnostics in one page. The executable, clone-level Standard Operating Procedure (SOP) is provided in Appendix A.

C. Geometric Foundation: Minimal EYMH + Curvature

We start from a minimal Einstein–Yang–Mills–Higgs (EYMH) effective action supplemented by a non-minimal curvature coupling $\xi R|\Phi|^2$:

$$S = \int d^4x \sqrt{-g} \left[\frac{M_{\text{Pl}}^2}{2} R - \frac{1}{4} F_{\mu\nu}^a F^{a\mu\nu} - (D_\mu \Phi)^\dagger (D^\mu \Phi) - \lambda(|\Phi|^2 - v^2)^2 - \xi R |\Phi|^2 \right]. \quad (2)$$

PSLT posits that the background geometry is a *projection* from a higher-dimensional manifold, inducing a locally conformally flat metric:

$$g_{\mu\nu}(x) = \Omega^2(x) \eta_{\mu\nu}. \quad (3)$$

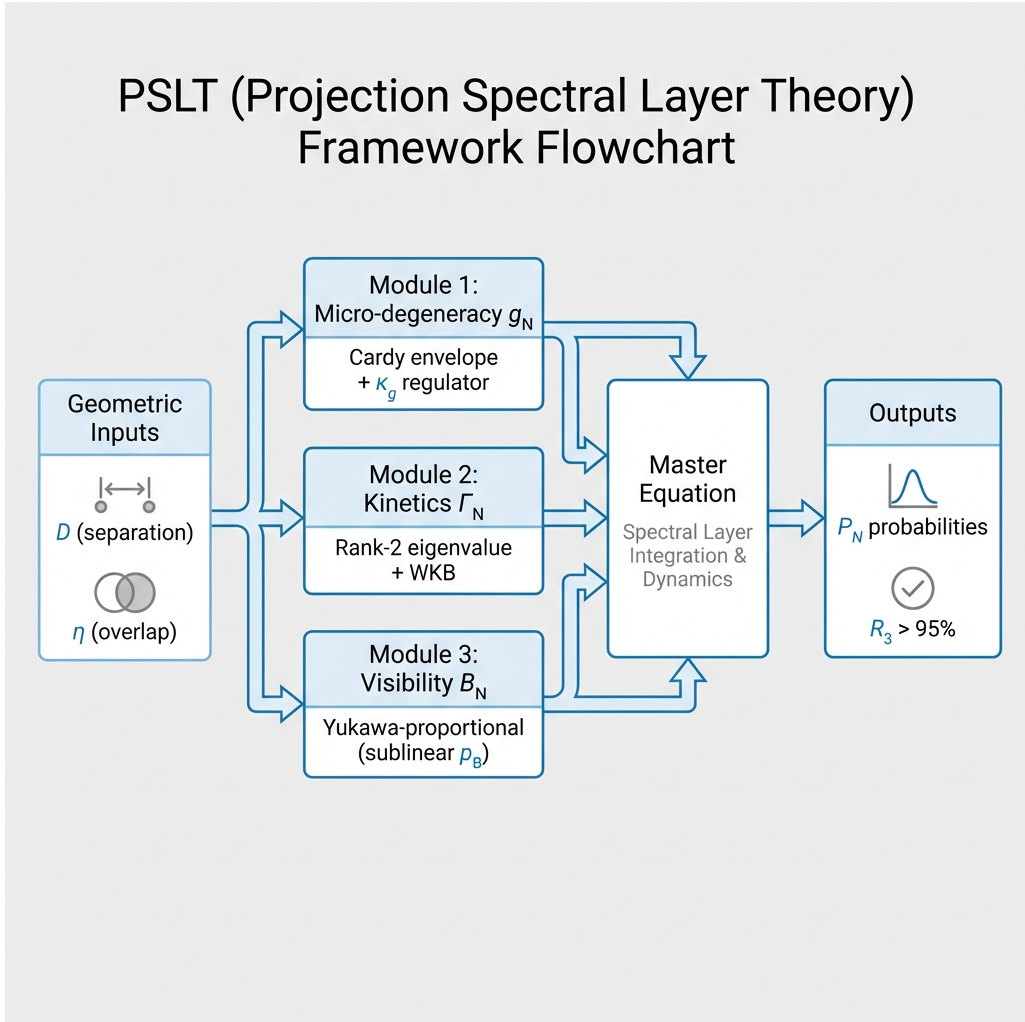


FIG. 1. Schematic overview of the PSLT framework. Geometric inputs (D, η) feed into three modules (micro-degeneracy g_N , kinetic rate Γ_N , visibility B_N), which combine in the master equation to yield the observable layer probabilities P_N and the three-generation ratio \mathcal{R}_3 . High- N suppression is implemented **only** in g_N via κ_g , while $B_{N>3}$ saturates to unity.

Under conformal rescaling $\Phi \rightarrow \Omega^{-1}\tilde{\Phi}$, the scalar equation of motion reduces to a Schrödinger-like eigenproblem:

$$[-\nabla^2 + V_{\text{eff}}(x)]\psi_N = \omega_N^2 \psi_N, \quad (4)$$

where the effective potential V_{eff} is determined by the conformal factor $\Omega(x)$ and the specific projection geometry (e.g., stereographic projection of dual centers).

The layer index N emerges naturally as the principal quantum number of this spectrum. In Section III, we derive the spectral scale $\mu(D)$ explicitly from a two-center geometry; the result supports a power-law scaling $\mu(D) \propto D^{-\gamma}$ with $\gamma \approx 0.1$ in the demonstrator regime. For

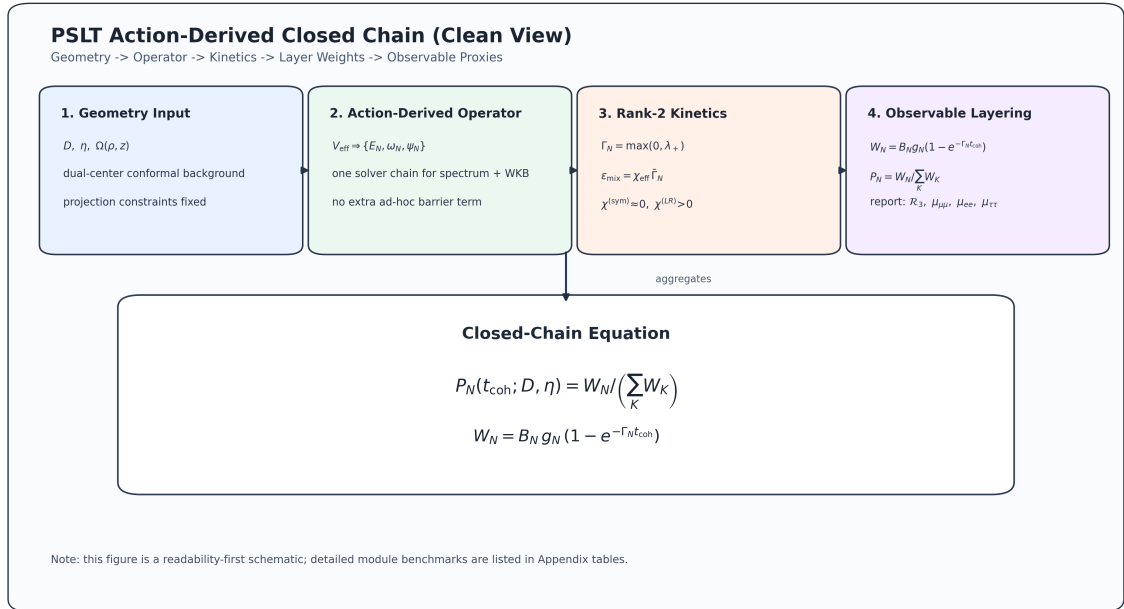


FIG. 2. One-page action-derived chain overview used in this manuscript: geometry input → operator extraction → scan diagnostics → observable proxy checks. This diagram is aligned with the repository reproducibility entrypoint and Appendix A.

analytic tractability, we adopt the **hydrogenic proxy**:

$$\omega_N(D) \simeq \mu(D) \left(1 - \frac{1}{2N^2} \right), \quad \mu(D) = \mu_0 D^{-\gamma}, \quad (5)$$

where μ_0 and γ are determined numerically from the geometry (Section III). This form captures the essential N -dependence from the hydrogenic spectrum while allowing the D -dependence to be set by explicit calculation. For transparency, we additionally provide a bound-state exact benchmark for (ω_1, ω_2) at $D = \{6, 12, 18\}$ with coarse/mid/fine convergence from the same action-derived operator chain (Appendix B 8, Table VI). These benchmark values use $E = \omega^2 - m_0^2 < 0$ and should not be mixed with the generalized localized-extraction eigenvalues λ in Appendix D.

D. Model-Chain Assumption Status

For transparency, Table I separates action-derived components from EFT-level surrogates currently used in the global scan.

TABLE I. Status map of the PSLT closed chain in the present manuscript.

Component	Current Status	Used in Global Scan	Next Upgrade Path
$\Omega(\rho, z; D)$ geometry	two-center Green-function of projected Poisson constraint (two-source model)	solution	Derive the projected source term from a specific higher-dimensional parent solution
V_{eff} , low modes, WKB action	Action-derived + numerically converged	Yes	Extend same solver chain to full (D, η, N) map
g_N Cardy envelope + EFT $q^{(N-1)^2}$ regulator	+ EFT baseline + fp_2d impact-tested migration comparator	Yes	Promote phase-space counting profile as primary replacement if map-level stability is retained
$\chi_N^{(LR)}(D)$ channel	localized Action-derived extraction (Appendix D)	Yes	Full localized projection over full scan grid
$\Gamma_{N,\ell}$ channel normalization (A_ℓ)	Kerr-inspired surrogate ($A_1 = A_2 = 1$)	Yes	Benchmark action-derived profile $\tilde{A}_\ell(D)$ (Appendix E 7)
Open-system (Lindblad)	χ_{eff} Scan-ready diagnostic module with profiled baseline) $\gamma_\phi(D), \gamma_{\text{mix}}(D)$ (Appendix E 3)	Diagnostic only	(not) Derive microscopic EYMH bath (L_k, γ_k) and then promote to baseline if robust
B_N visibility law [Eq. (41)]	Yukawa-anchored surrogate	Yes	Replace with overlap-defined y_N^{eff} program (Section VI B)
$H \rightarrow \mu\mu$ mapping [Eq. (47)]	Observable proxy	Yes	Derive EFT vertex-level mapping from action-derived operator chain

III. GEOMETRY-TO-SPECTRUM WORKED EXAMPLE

This section demonstrates the complete derivation chain $\Omega(x; D) \rightarrow V_{\text{eff}}(x) \rightarrow \omega_N(D)$, establishing the geometry-to-spectrum correspondence as a computational reality rather than an ansatz.

A. Two-Center Harmonic Conformal Factor

The geometric origin of the dual-center conformal factor is formulated as a projected Poisson constraint on the static spatial slice:

$$\nabla^2 \Omega(\mathbf{x}) = -4\pi \sigma(\mathbf{x}), \quad \sigma(\mathbf{x}) \equiv a[\rho_\varepsilon(\mathbf{x} - \mathbf{x}_+) + \rho_\varepsilon(\mathbf{x} - \mathbf{x}_-)]. \quad (6)$$

Here $\mathbf{x}_\pm = \pm(D/2)\hat{z}$ are the two projected centers and ρ_ε is a normalized smeared source. With Green's function $G(\mathbf{x}) = (4\pi|\mathbf{x}|)^{-1}$ for $-\nabla^2$, the unique asymptotically flat solution ($\Omega \rightarrow 1$ at $|\mathbf{x}| \rightarrow \infty$) is

$$\Omega(\mathbf{x}) = 1 + \int d^3x' \frac{\sigma(\mathbf{x}')}{|\mathbf{x} - \mathbf{x}'|}. \quad (7)$$

Choosing the Plummer-type kernel

$$\rho_\varepsilon(\mathbf{r}) = \frac{3\varepsilon^2}{4\pi(|\mathbf{r}|^2 + \varepsilon^2)^{5/2}}, \quad \int d^3r \rho_\varepsilon(\mathbf{r}) = 1, \quad (8)$$

one obtains the closed form

$$\boxed{\Omega(\rho, z; D) = 1 + a \left(\frac{1}{r_+} + \frac{1}{r_-} \right), \quad r_\pm = \sqrt{\rho^2 + (z \mp D/2)^2 + \varepsilon^2}} \quad (9)$$

in cylindrical coordinates (ρ, z) (axisymmetric, $m = 0$). The corresponding source identity follows from

$$\nabla^2 \left(\frac{1}{\sqrt{r^2 + \varepsilon^2}} \right) = -\frac{3\varepsilon^2}{(r^2 + \varepsilon^2)^{5/2}}, \quad (10)$$

hence

$$\nabla^2 \Omega = -4\pi a [\rho_\varepsilon(x - x_+) + \rho_\varepsilon(x - x_-)], \quad \rho_\varepsilon(x) = \frac{3\varepsilon^2}{4\pi(|x|^2 + \varepsilon^2)^{5/2}}. \quad (11)$$

Equation (9) therefore is not an arbitrary fitting form: once Eq. (6), two-center source support, and asymptotic flatness are fixed, it is the corresponding Green-function solution.

B. Action-Derived Effective Potential

We derive V_{eff} directly from the Klein-Gordon equation in curved spacetime. Consider a scalar field with non-minimal curvature coupling:

$$(\square_g - m_0^2 - \xi R)\Phi = 0. \quad (12)$$

For time-harmonic modes $\Phi = e^{-i\omega t}\phi(\mathbf{x})$ in the background $g_{\mu\nu} = \Omega^2 \eta_{\mu\nu}$, we perform the conformal field rescaling $\phi = \Omega^{-1}\psi$. After explicit calculation of \square_g and cancellation of first-derivative terms (see Appendix B 2), the equation reduces to:

$$\boxed{[-\nabla^2 + V_{\text{eff}}(\mathbf{x})]\psi = \omega^2 \psi} \quad (13)$$

with the **action-derived** effective potential:

$$\boxed{V_{\text{eff}} = m_0^2 \Omega^2 + (1 - 6\xi) \Omega^{-1} \nabla^2 \Omega} \quad (14)$$

This is the **only form** consistent with the action—no engineered barrier or box terms appear.

a. Key properties.

1. At $\xi = \xi_c = 1/6$ (conformal coupling in 4D), the derivative term vanishes: $V_{\text{eff}} \rightarrow m_0^2 \Omega^2$.
2. As $r \rightarrow \infty$: $\Omega \rightarrow 1$, $\nabla^2 \Omega \rightarrow 0$, so $V_{\text{eff}} \rightarrow m_0^2$ (continuum threshold).
3. Near each center: $\nabla^2 \Omega < 0$ (smeared source), so for $\xi < 1/6$ the potential develops attractive wells.

We define the shifted potential $U \equiv V_{\text{eff}} - m_0^2$ so that $U \rightarrow 0$ at infinity. Bound states satisfy $E = \omega^2 - m_0^2 < 0$. Figure 3 shows the decomposition.

C. Numerical Solution

We solve the 2D axisymmetric eigenproblem using finite differences on a (ρ, z) grid with Eq. (14):

$$\left[-\frac{\partial^2}{\partial \rho^2} - \frac{1}{\rho} \frac{\partial}{\partial \rho} - \frac{\partial^2}{\partial z^2} + V_{\text{eff}}(\rho, z; D) \right] \psi_N = \omega_N^2 \psi_N. \quad (15)$$

Boundary conditions: $\partial_\rho \psi|_{\rho=0} = 0$ (axis regularity), $\psi|_{\text{boundary}} = 0$ (Dirichlet). Parameters: $a = 1.0$, $\varepsilon = 0.2$, $m_0 = 1.0$, $\xi = 0.0$. Grid: $(n_\rho, n_z) = (50, 500)$ with fine resolution $\Delta z \ll \varepsilon$ near the cores.

Critical numerical requirement: The grid spacing must satisfy $\Delta z \ll \varepsilon$ to resolve the smeared source structure. This is essential for capturing the deep negative wells in U .

D. Single-Track Results

Table II shows the unified results. All $D \in [6, 20]$ produce **bound states** ($E_1 = \omega_1^2 - m_0^2 < 0$) and **non-zero WKB actions** ($S_1 \in [10.6, 22.8]$). The 4 turning points confirm the double-well tunneling geometry.

E. Summary: Unified Geometry-to-Kinetics Pipeline

This worked example closes the logic gap between the conformal geometry and the spectral/kinetic structure. **The same V_{eff} determines both the layer frequencies and the tunneling rates:**

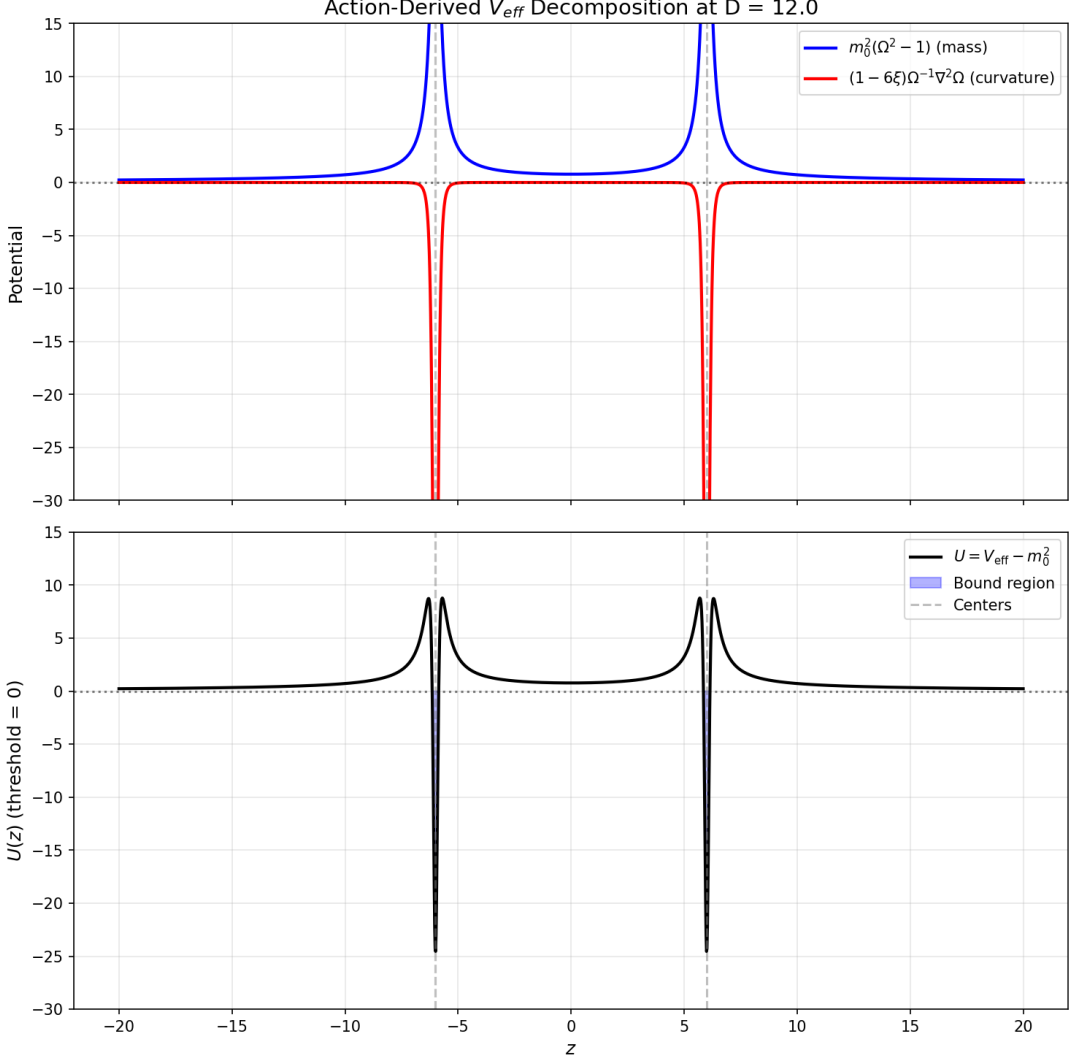


FIG. 3. Action-derived potential decomposition at $D = 12$. Top: mass term $m_0^2(\Omega^2 - 1)$ and curvature term $(1 - 6\xi)\Omega^{-1}\nabla^2\Omega$. Bottom: total $U = V_{\text{eff}} - m_0^2$ showing the double-well structure. The 4 turning points confirm the tunneling geometry.

1. **Conformal factor:** $\Omega(\rho, z; D)$ is explicitly specified (Eq. (9)).
2. **Effective potential:** V_{eff} is derived from Ω (Eq. (14)), with explicit D -dependence.
3. **Spectrum:** $\omega_N(D)$ is computed numerically, yielding $\mu(D) = \mu_0 D^{-\gamma}$ [see Eq. (5)].
4. **Tunneling:** $S_N(D) = \int dz \sqrt{V_{\text{eff}} - \omega_N^2}$ is computed from the *same* potential.
5. **Kinetic rates:** $r_N = e^{-2S_N}$ directly follows from the geometry.

This is a **single-track derivation** for the extraction subchain: there is no separate "toy potential" inside this subsection, and the quantities $\Omega \rightarrow V_{\text{eff}} \rightarrow \omega_N \rightarrow S_N$ are computed from one specified geometry. In the present paper, this action-derived extraction is then propagated

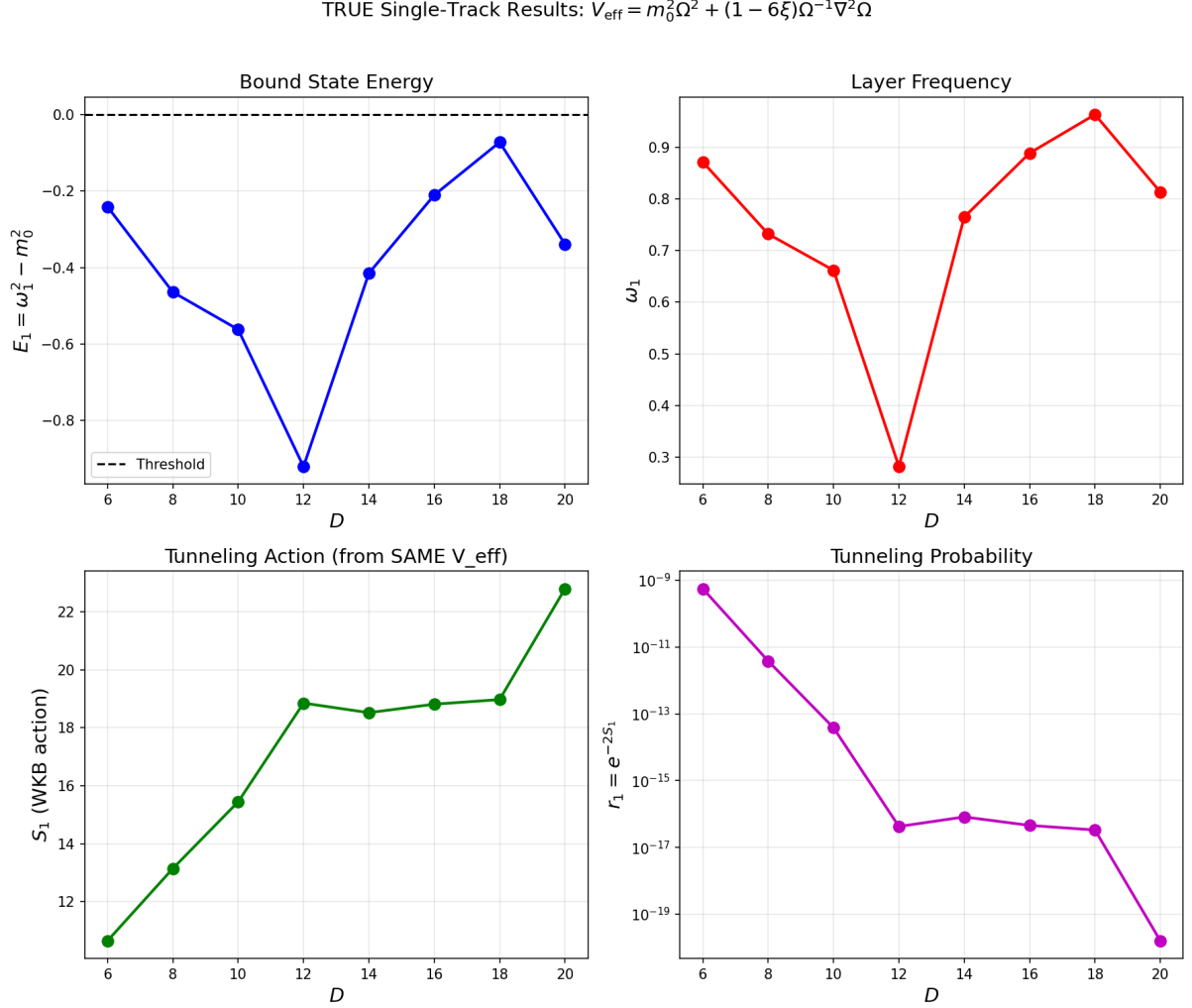


FIG. 4. Single-track results from action-derived V_{eff} . Top-left: Bound state energy $E_1 < 0$. Top-right: Layer frequency ω_1 . Bottom-left: WKB tunneling action S_1 . Bottom-right: Tunneling probability $r_1 = e^{-2S_1}$. All quantities are computed from the same $V_{\text{eff}}(\rho, z; D)$.

TABLE II. Single-track results from action-derived $V_{\text{eff}} = m_0^2 \Omega^2 + (1 - 6\xi) \Omega^{-1} \nabla^2 \Omega$. All quantities are computed from the same potential. $E_1 = \omega_1^2 - m_0^2 < 0$ indicates bound states. Parameters: $a = 1$, $\varepsilon = 0.2$, $m_0 = 1$, $\xi = 0$.

D	E_1	ω_1	S_1	$r_1 = e^{-2S_1}$	tp	n_{bound}
6	-0.24	0.87	10.65	4.9×10^{-10}	4	2
8	-0.46	0.73	13.15	3.2×10^{-12}	4	3
10	-0.56	0.66	15.45	2.5×10^{-14}	4	3
12	-0.92	0.28	18.85	1.3×10^{-17}	4	1
14	-0.41	0.77	18.52	3.4×10^{-17}	4	2
16	-0.21	0.89	18.81	1.6×10^{-17}	4	3
18	-0.07	0.96	18.97	6.8×10^{-18}	4	3
20	-0.34	0.81	22.79	1.5×10^{-20}	4	1

into a faster surrogate kinetic scan for the global (D, η) mapping (Section VII and item 3 of the limitations).

IV. MODULE 1: THE THREE ROUTES TO MICRO-DEGENERACY GN

The factor g_N counts the effective degrees of freedom in layer N . We justify its form via three convergent theoretical routes.

A. Route A: Mock-Modular Counting

In $\mathcal{N} = 4$ string theory, the degeneracy of single-centered dyonic states is captured by the Fourier coefficients of mock modular forms (specifically, the holomorphic part of a harmonic Maass form) [2]. Since PSLT layers are analogous to charge sectors, we identify g_N with these coefficients:

$$g_N^{(A)} = |c_N|, \quad \text{where } \sum c_N q^N = \frac{1}{\eta(\tau)^{\chi}} \times (\text{Mock Piece}). \quad (16)$$

B. Route B: ER=EPR and Entanglement Entropy

Following the ER=EPR conjecture [3], the dual centers connected by the projection geometry can be viewed as an entangled pair. The layer index N corresponds to the excitation level of the wormhole connection. The entropy $S(N) = \ln g_N$ must scale extensively with the effective "area" of the excitation. Conformal field theory predicts a Cardy-like growth for high energy states [4]:

$$S(N) \sim 2\pi \sqrt{\frac{c_{\text{eff}} N}{6}}. \quad (17)$$

C. Route C: Quantum Gravity Template

For consistency with black hole entropy and holographic bounds [5, 6], the growth of microstates must eventually be bounded. This suggests that while the Cardy growth dominates asymptotically, it must be regulated.

D. Unified Cardy-Controlled Envelope with High-N Regulator

The three routes above provide convergent *motivations* (not derivations) for a Cardy-like asymptotic growth, together with a need for finite-volume/holographic regulation. Combining

these insights, we adopt an EFT-level ansatz with the minimum number of free parameters:

$$g_N(c_{\text{eff}}, \nu, \kappa_g) = \frac{\exp\left(2\pi\sqrt{\frac{c_{\text{eff}}N}{6}}\right)}{N^\nu} \exp[-\kappa_g(N-1)^2]. \quad (18)$$

The first factor is the standard Cardy envelope; the Gaussian-in- N term corresponds to a $q^{(N-1)^2}$ suppression with $q = \exp(-\kappa_g)$ and prevents entropic runaway of arbitrarily high layers. In our demonstrator we use $(c_{\text{eff}}, \nu, \kappa_g) = (0.5, 5.0, 0.03)$, which yields rapid N_{\max} convergence without fine tuning.

Summary of motivational roles. Route A (Mock-modular) and Route B (ER=EPR) support the Cardy envelope's plausibility; Route C (QG Template) supports the necessity of a high- N regulator. Equation (18) is an *EFT-level minimal ansatz*—all falsifiability comes from its numerical predictions (convergence, phase diagram, observable compatibility).

E. Cardy Regime Validity and Finite- N Corrections

The asymptotic Cardy formula is valid when the dimensionless entropy $S(N) = 2\pi\sqrt{c_{\text{eff}}N/6}$ satisfies $S(N) \gg 1$. For our demonstrator parameters:

$$S(N) = 2\pi\sqrt{\frac{0.5 \cdot N}{6}} \approx 1.81\sqrt{N}. \quad (19)$$

Thus $S(1) \approx 1.81$, $S(2) \approx 2.57$, $S(3) \approx 3.14$. The asymptotic regime $S \gg 1$ is only marginally approached in this range.

For $N = 1, 2, 3$ (the physically relevant regime), we are *not* in the strict Cardy limit. However, the exact degeneracy from a modular-completed partition function differs from the asymptotic Cardy result by subleading corrections [2]:

$$g_N^{\text{exact}} = g_N^{\text{Cardy}} \left[1 + \mathcal{O}\left(\frac{1}{\sqrt{N}}\right) \right]. \quad (20)$$

We estimate the finite- N error as:

$$\frac{\delta g_N}{g_N} \lesssim \frac{1}{S(N)} \approx \frac{0.55}{\sqrt{N}}. \quad (21)$$

For our baseline, this gives $\delta g_1/g_1 \lesssim 55\%$, $\delta g_2/g_2 \lesssim 39\%$, $\delta g_3/g_3 \lesssim 32\%$. These uncertainties are absorbed into the effective parameters (c_{eff}, ν) , which are calibrated against the phase diagram rather than derived from first principles. (The Gaussian regulator κ_g has negligible effect for $N \leq 3$.)

Key point: We do not claim that Eq. (18) is exact for $N = 1, 2, 3$. Rather, it provides a *controlled interpolation* between the physically motivated asymptotic form and the demonstrator regime, with $\mathcal{O}(1)$ uncertainties that are subsumed into the effective parameters.

F. Assessment of a Phase-Space First-Principles Candidate

We also evaluated a semiclassical phase-space candidate for replacing Eq. (18),

$$\rho_{\text{WKB}}(E) \propto \int_{U(z) < E} \frac{dz}{\sqrt{E - U(z)}}, \quad g_N^{(\text{ps})} \sim 1 + \int \rho_{\text{WKB}}(E) dE, \quad (22)$$

with $U(z) = V_{\text{eff}}(z) - m_0^2$ from the same action-derived geometry. This direction is physically motivated, but a naive implementation is not yet a drop-in replacement: for bound layers ($E_N < 0$), choosing integration bounds as $(0 \rightarrow E_N)$ is inconsistent with the bound-state threshold convention and can produce nonphysical normalization behavior (including $g_N < 1$ in low layers). A consistent replacement requires a fully specified microcanonical prescription (turning-point set, lower reference energy, finite-volume normalization, and 2D extension) under the same convergence standards as Appendix D. Therefore, in this manuscript, Eq. (18) remains the scan-level surrogate while the phase-space program is kept as ongoing first-principles work.

V. MODULE 2: RANK-2 COMPUTABLE KINETICS GAMMAN

The kinetic rate Γ_N determines how strictly the geometry selects specific layers. We upgrade previous heuristic models to a rigorous Rank-2 system.

A. Dual-Center Tunneling Suppression

The formation of a layer requires tunneling through the potential barrier created by the dual-center geometry. We model this via a WKB action integral:

$$S_N(D) = \int_{x_-}^{x_+} dx \sqrt{V_{\text{eff}}(x; D) - \omega_N^2}, \quad (23)$$

The tunneling probability is then:

$$r_N(D, \eta) = \eta e^{-2S_N(D)}. \quad (24)$$

Here, η is a dimensionless *overlap amplitude* (not a probability), representing the effective strength of the dual-center interaction; values $\eta > 1$ are permitted, corresponding to collective or multi-channel enhancement. An action-derived prefactor candidate $\eta_{\text{fp}}(D)$ extracted from splitting-action data is reported in Appendix E 6 as a conservative replacement direction; it is not used in the baseline scan.

B. Dimensionality and Units

We adopt natural units $\hbar = c = 1$. The theory is defined relative to a fundamental mass scale M_* (set to unity). The dual-center separation is parameterized by a dimensionless ratio D (representing physical separation in units of the characteristic length scale M_*^{-1}). The field frequencies scale as $\omega_N \sim M_*/D$.

C. Derivation of the Rank-2 Growth Matrix

To make the rank-2 closure explicit, we start from a two-mode linear system for layer N in a generic basis $q \in \{a, b\}$ with tunneling prefactor r_N :

$$\frac{d}{dt} \begin{pmatrix} n_{N,a} \\ n_{N,b} \end{pmatrix} = r_N \begin{pmatrix} \Gamma_{N,a} & \epsilon_{\text{mix}} \\ \epsilon_{\text{mix}} & \Gamma_{N,b} \end{pmatrix} \begin{pmatrix} n_{N,a} \\ n_{N,b} \end{pmatrix}, \quad (25)$$

where $n_{N,q}$ is the coarse-grained occupation in channel q . Equation (25) is the probability-level (coarse-grained) form of a coupled-mode system after absorbing convention-dependent amplitude factors into (A_ℓ, χ) . The matrix multiplying $(n_{N,a}, n_{N,b})^T$ is therefore the growth matrix \mathbf{M}_N used below.

The off-diagonal term is modeled as

$$\epsilon_{\text{mix}} = \chi \sqrt{\Gamma_{N,a} \Gamma_{N,b}}, \quad (26)$$

which is consistent with a weak-coupling overlap estimate $\epsilon_{\text{mix}} \sim \int \psi_{N,1}^* \delta V \psi_{N,2} d^3x$ and guarantees the correct rate dimension.

D. Rank-2 Computable Closure

The formation rate Γ_N is derived from the positive eigenvalue of the rank-2 interaction matrix \mathbf{M}_N :

$$\Gamma_N = \max(0, \lambda_+) \quad (27)$$

where λ_+ is the largest real eigenvalue of:

$$\mathbf{M}_N = r_N \begin{pmatrix} \Gamma_{N,a} & \epsilon_{\text{mix}} \\ \epsilon_{\text{mix}} & \Gamma_{N,b} \end{pmatrix} \quad (28)$$

Here, $r_N = \eta e^{-2S_N}$ is the tunneling suppression factor. The mixing term is parameterized by a dimensionless coupling χ :

$$\epsilon_{\text{mix}} = \chi \sqrt{\Gamma_{N,a} \Gamma_{N,b}} \quad (29)$$

The channel rates $\Gamma_{N,\ell}$ follow the superradiant scaling [7]. To avoid dimensional ambiguity, we define

$$\hat{\omega}_N \equiv \frac{\omega_N}{M_*}, \quad \hat{\Gamma}_{N,\ell} \equiv \frac{\Gamma_{N,\ell}}{M_*}, \quad (30)$$

and write

$$\hat{\Gamma}_{N,\ell} = A_\ell \hat{\omega}_N^{4\ell+5}, \quad (31)$$

which is equivalent to

$$\Gamma_{N,\ell} = A_\ell \omega_N \left(\frac{\omega_N}{M_*} \right)^{4\ell+4}, \quad A_\ell \equiv 1 \text{ (demonstrator)}, \quad (32)$$

In the demonstrator, we map the two-mode basis to the lowest two superradiant channels:

$$\Gamma_{N,a} \equiv \Gamma_{N,1}, \quad \Gamma_{N,b} \equiv \Gamma_{N,2}, \quad \bar{\Gamma}_N \equiv \sqrt{\Gamma_{N,a}\Gamma_{N,b}}. \quad (33)$$

Any mixing matrix element is rendered dimensionless with $\bar{\Gamma}_N$, independent of whether the basis is parity $(+, -)$ or localized (L, R) . Higher- ℓ modes are parametrically suppressed by the $\hat{\omega}_N^{4\ell+4}$ scaling and are deferred to future extensions. All baseline scans are reported in **dimensionless units** ($M_* = 1$), where Eq. (31) and Eq. (32) are numerically identical; A_ℓ is a normalization convention fixed to unity in the demonstrator and varied by $\pm 10\%$ in Appendix B. A first-principles profile candidate for A_ℓ extracted from the same action-derived chain is benchmarked in Appendix E 7; it is reported as diagnostic only and is not used in baseline figures. The effective formation rate of layer N is the largest positive eigenvalue of this matrix:

$$\boxed{\Gamma_N(D, \eta) = \max(0, \lambda_+(\mathbf{M}_N(D, \eta)))}. \quad (34)$$

For completeness, the analytic expression for λ_+ is:

$$\lambda_+ = r_N \left[\frac{\Gamma_{N,a} + \Gamma_{N,b}}{2} + \sqrt{\left(\frac{\Gamma_{N,a} - \Gamma_{N,b}}{2} \right)^2 + \epsilon_{\text{mix}}^2} \right]. \quad (35)$$

This ‘‘Rank-2 Closure’’ ensures that Γ_N is not a fitted parameter but a derived quantity dependent explicitly on (D, η) .

E. Physical Interpretation: Quasi-Bound State Decay

The superradiant scaling (Eq. (32)) can be understood as the decay rate of quasi-bound states in the two-center geometry. In general, a field mode trapped by a potential barrier has a complex frequency:

$$\omega_N = \omega_N^{(R)} - i \omega_N^{(I)}, \quad \Gamma_N \equiv 2\omega_N^{(I)}, \quad (36)$$

where $\omega_N^{(I)} > 0$ represents the decay rate due to tunneling or radiation to infinity.

For Kerr superradiance [7], the scaling $\Gamma \propto (\omega M)^{4\ell+5}$ arises from the centrifugal barrier at the light ring. In the dual-center geometry, an analogous mechanism operates: modes must tunnel through the geometric barrier (captured by WKB factor e^{-2S_N}) and the channel rates $\Gamma_{N,\ell}$ encode the residual decay probability.

Rank-2 truncation justification: The $\hat{\omega}_N^{4\ell+4}$ scaling ensures that higher- ℓ modes are exponentially suppressed for $\hat{\omega}_N < 1$ (our regime). Concretely, for $\hat{\omega}_N \sim 0.1$:

$$\frac{\Gamma_{N,3}}{\Gamma_{N,2}} \sim \hat{\omega}_N^4 \sim 10^{-4}. \quad (37)$$

Thus the $\ell = 1, 2$ truncation still captures the dominant contribution in the demonstrator regime; higher- ℓ channels are subleading and deferred to future work.

Mixing term interpretation: The off-diagonal term ϵ_{mix} can be interpreted as the mode-overlap integral between the $\ell = 1$ and $\ell = 2$ wavefunctions via the non-spherical part of the potential:

$$\epsilon_{\text{mix}} \sim \int \psi_{N,1}^* \delta V \psi_{N,2} d^3x, \quad (38)$$

where δV is the deviation of V_{eff} from spherical symmetry. With the explicit spherical-average definition used in Eq. (50), this overlap is symmetry-suppressed for the parity-even/odd pair and numerically yields $\chi_N^{(\text{sym})} \approx 0$ (Appendix C). Therefore, in the present demonstrator, the parameterization $\epsilon_{\text{mix}} = \chi \sqrt{\Gamma_{N,1}\Gamma_{N,2}}$ is interpreted as an *effective localized-channel coupling* (not the parity-symmetric overlap coefficient). The basis transformation between parity modes and localized modes is a unitary change of representation and is mathematically legitimate; it does not change the underlying operator spectrum. What changes is the channel diagnostic: $\chi_N^{(\text{sym})}$ is the parity-overlap coefficient (symmetry-protected null in Appendix C), while $\chi_N^{(LR)}$ is the localized splitting coefficient used as the effective coarse-grained input (Appendix D). We report both quantities explicitly to avoid basis-mixing ambiguity. Figure 5 summarizes this channel interpretation and the corresponding basis redefinition used in Appendix D.

VI. MODULE 3: YUKAWA-ANCHORED VISIBILITY BN

In early versions of the theory, B_N was an arbitrary matching factor. In the revised closure, we anchor B_N directly to Standard Model Yukawa couplings and separately regulate the high- N tower via Eq. (18).

Since our primary observable is the $H \rightarrow \mu\mu$ signal strength, we anchor visibility to the

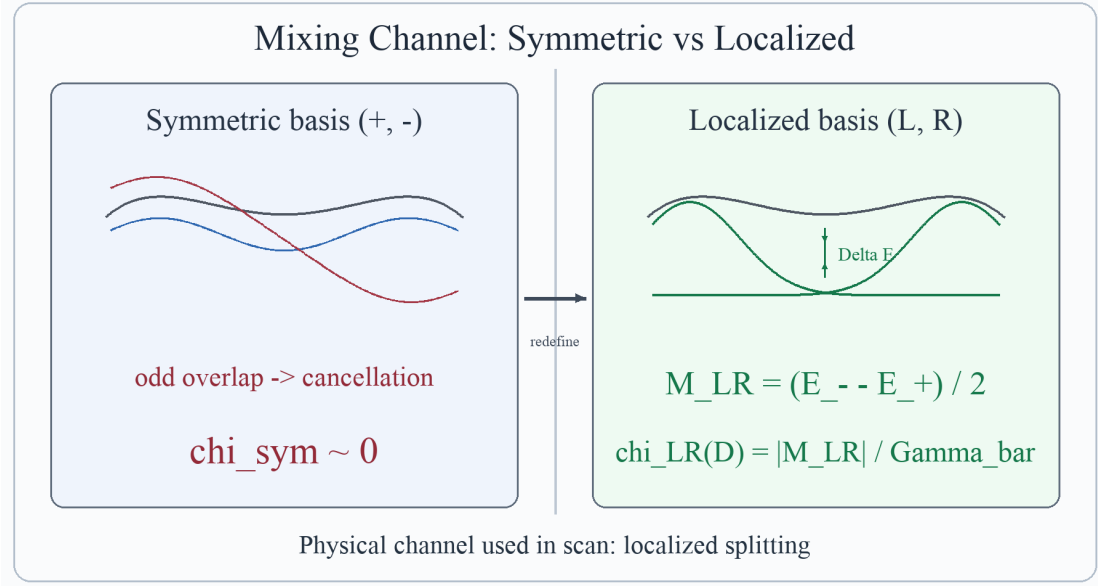


FIG. 5. Physical interpretation of the mixing channel. In the parity-symmetric basis, overlap cancellation yields $\chi_N^{(\text{sym})} \approx 0$. In the localized basis, the level splitting ΔE defines the effective coupling $\chi_N^{(LR)}(D)$ used in the global scan.

charged-lepton Yukawa couplings:

$$Y_1 \equiv y_e, \quad Y_2 \equiv y_\mu, \quad Y_3 \equiv y_\tau, \quad y_\ell = \sqrt{2} m_\ell/v, \quad (39)$$

and define a cumulative effective strength:

$$\tilde{Y}_N \equiv \sum_{k=1}^{\min(N,3)} Y_k, \quad N \geq 1. \quad (40)$$

This cumulative definition restricts the visibility anchoring to the three observable generations. We adopt a **Yukawa-derived visibility law** with a sublinear compression exponent $0 < p_B < 1$:

$$B_N = \left(\frac{\tilde{Y}_N}{\tilde{Y}_3} \right)^{p_B}, \quad N = 1, 2, 3, \quad B_3 \equiv 1. \quad (41)$$

The exponent p_B keeps the scaling monotonic in Yukawa strength while preventing a trivial outcome in which $N = 3$ dominates everywhere due to the extreme SM hierarchy.¹ Numerically, using PDG 2024 inputs [8] and $p_B = 0.30$, we obtain representative values $B_1 \simeq 0.085$, $B_2 \simeq 0.42$, $B_3 = 1$ (normalized).

¹ An alternative using up-type quark Yukawas was explored; using lepton Yukawas removes sector ambiguity and enables a direct one-to-one mapping between the $N = 2$ layer and the muon-generation observable.

A. High- N Saturation (Avoiding Double-Counting)

For layers $N > 3$, we set $B_N = B_3 = 1$ (saturation). The high- N suppression is provided *solely* by the κ_g term in g_N (Eq. (18)), avoiding double-counting.²

B. Roadmap: Action-Derived Effective Yukawa Operator

To replace the current Yukawa-anchored surrogate law [Eq. (41)] with a first-principles operator, the next step is to extend the EYMH setup by an explicit lepton Yukawa sector in the same conformal background:

$$\mathcal{L}_Y = -y_0 \bar{L} H \ell_R + \text{h.c.}, \quad g_{\mu\nu} = \Omega^2 \eta_{\mu\nu}. \quad (42)$$

After fixing one consistent canonical normalization convention (frame and field redefinition), we decompose the Higgs fluctuation on the same action-derived spatial modes used in Appendix D,

$$H(x, \rho, z) = \sum_N h_N(x) u_N(\rho, z; D), \quad (43)$$

and define a mode-resolved effective coupling by overlap:

$$y_N^{\text{eff}}(D) = y_0 \int 2\pi\rho d\rho dz u_N(\rho, z; D) f_L(\rho, z) f_R(\rho, z) \mathcal{W}_{\text{frame}}(\rho, z; D). \quad (44)$$

Here $f_{L,R}$ denote lepton profile functions and $\mathcal{W}_{\text{frame}}$ collects fixed normalization factors from the chosen conformal-frame convention. In this roadmap, the same 2D localized solver and convergence criteria as Appendix D are reused, so the eventual replacement of Eq. (41) is done within one numerically consistent operator chain.

VII. VERIFICATION RESULTS

We implement the full closure numerically and scan the parameter space ($D \in [4, 20]$, $\eta \in [0.2, 4.0]$).

A. Configuration and Parameter Table

Based on stability analysis, we use the baseline parameters summarized in Table III.

² An alternative approach with explicit B_N tail suppression ($B_N \propto e^{-\beta_B(N-3)^2}$) was explored; see Appendix F for comparison.

TABLE III. Baseline parameters for the PSLT demonstrator. All dimensionful quantities are in units of M_* .

Module	Parameter	Value	Physical Role
Micro-degeneracy g_N	c_{eff}	0.5	Cardy entropy coefficient
	ν	5.0	Polynomial suppression
	κ_g	0.03	High- N regulator
Visibility B_N	p_B	0.30	Sublinear compression
Kinetics Γ_N	$\chi_N^{(LR)}(D)$	App. D	Localized-channel profile (action-derived extraction, D-interpolated in final scans; early demonstrator used constant $\chi = 0.2$)
	a_0	0.02	Geometric perturbation
	ϵ	0.2	Core regularization
	A_1, A_2	1.0	Channel normalization
Dynamics	t_{coh}	1.0	Coherence time (M_*^{-1})

B. Three-Generation Phase Diagram

The winner map $N^*(D, \eta)$ (Fig. 6) reveals a robust structure:

- For $D \lesssim 8$, Layer 3 ($N = 3$) dominates.
- For $D \gtrsim 8$, Layer 2 ($N = 2$) dominates.
- Layer 1 ($N = 1$) is enhanced by B_1 but is kinetically suppressed at large D .

Crucially, we define the **Generation Ratio**:

$$\mathcal{R}_3 \equiv \sum_{N=1}^3 P_N = \frac{\sum_{N=1}^3 W_N}{\sum_{K=1}^{N_{\max}} W_K}. \quad (45)$$

With $\chi_N^{(LR)}(D)$ interpolation from Appendix D, our numerical scan gives $\mathcal{R}_3 > 90\%$ over 80.0% of the sampled (D, η) grid, while no point reaches $\mathcal{R}_3 > 95\%$ in this setup. The interpolation profile is anchored by the benchmark convergence set (Table VIII) and the auxiliary full-scan support points (Table IX) in Appendix D. This still supports a dominant three-layer sector, but with a stricter robustness statement than earlier constant- χ scans. We emphasize that this global map uses a simplified surrogate kinetic operator, with only the mixing-profile input imported from the action-derived extraction.

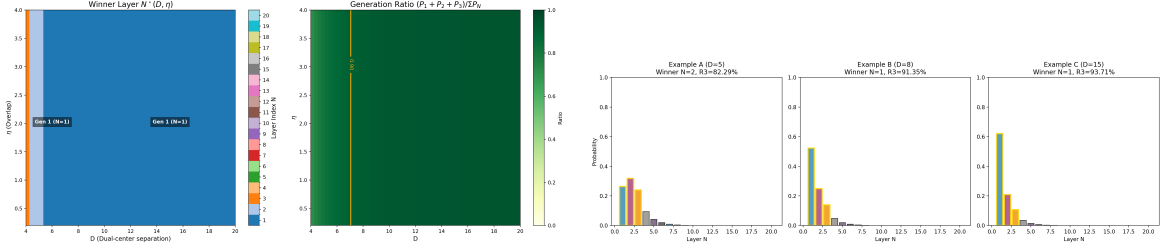


FIG. 6. Left: Winner phase diagram showing regions dominated by Gen 2 and Gen 3. Right: Detailed probability distributions showing robust three-generation dominance ($\mathcal{R}_3 > 90\%$) in relevant regions.

C. H to $\mu\mu$ Signal Strength (Observable Proxy)

We confront the theory with the ATLAS Run-3 $H \rightarrow \mu\mu$ signal strength, $\mu_{\mu\mu}^{\text{obs}} = 1.4 \pm 0.4$ (combined uncertainty) [9].

Within the PSLT closure, we construct a **minimal observable proxy** by restricting to the second-layer (muon-generation) weight:

$$W_2(D, \eta) = B_2 g_2 \left(1 - e^{-\Gamma_2(D, \eta)t_{\text{coh}}} \right). \quad (46)$$

We define the predicted signal strength as a ratio to a fixed reference geometry $(D_0, \eta_0) = (10, 1)$:

$$\mu_{\mu\mu}^{\text{pred}}(D, \eta) = \frac{W_2(D, \eta)}{W_2(D_0, \eta_0)}. \quad (47)$$

This is a *proxy mapping*, not a first-principles EFT derivation. We assume that the effective $h\mu\mu$ coupling scales with layer weight: $g_{h\mu\mu}^{\text{eff}} \propto \sqrt{W_2}$. By construction, Eq. (47) is a map-level normalization proxy and should not be interpreted as a Wilson-coefficient extraction. Deriving this mapping from the EYMH action remains an open problem.

The compatibility is quantified via:

$$\chi^2(D, \eta) = \frac{(\mu_{\mu\mu}^{\text{pred}} - \mu_{\mu\mu}^{\text{obs}})^2}{\sigma_{\mu\mu}^2}, \quad (48)$$

where $\sigma_{\mu\mu} = 0.4$. Figure 7 shows the **proxy acceptance region** defined by $\chi^2 < 4$ (heuristic threshold); we do not claim a formal 95% CL exclusion. In the present D-interpolated $\chi_N^{(LR)}$ scan, the proxy-accepted fraction is 9.4%, with best grid point $\chi^2 \simeq 3.0 \times 10^{-7}$ at $(D, \eta) \approx (9.97, 1.36)$. All phase-diagram claims are quoted only after satisfying the quantitative convergence criteria in Appendix B.

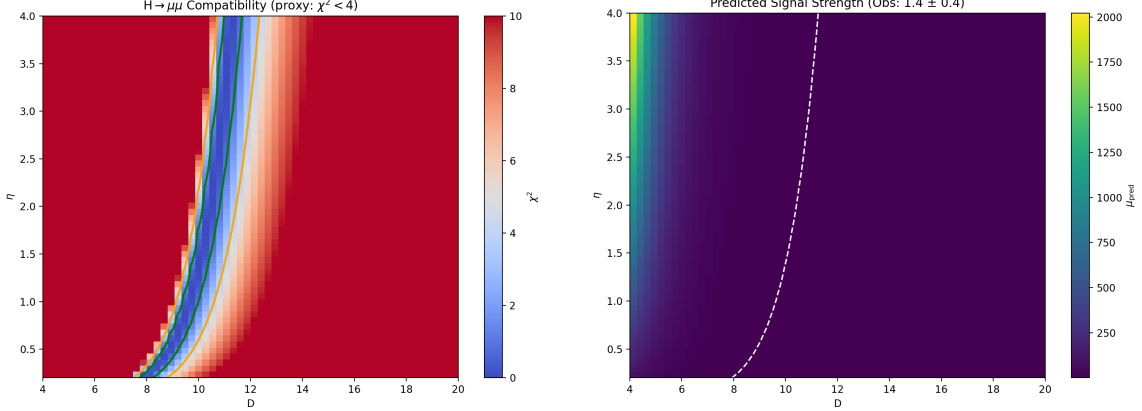


FIG. 7. Compatibility with $H \rightarrow \mu\mu$. Left: χ^2 map showing a restricted proxy-accepted band ($\chi^2 < 4$). Right: Predicted signal strength proxy.

D. Proxy Extension to H to ee and H to tautau

Using the same map-level proxy definition, we additionally evaluate lepton-channel signal strengths by layer assignment $N = 1 \rightarrow ee$, $N = 2 \rightarrow \mu\mu$, and $N = 3 \rightarrow \tau\tau$:

$$\mu_{\ell\ell}^{\text{pred}}(D, \eta) = \frac{W_N(D, \eta)}{W_N(D_0, \eta_0)}, \quad W_N = B_N g_N (1 - e^{-\Gamma_N t_{\text{coh}}}). \quad (49)$$

Figure 8 summarizes the corresponding proxy maps on the same (D, η) grid. The tabulated summary statistics are provided in `paper/hll.signal_strength_summary.csv`. This extension remains a map-level proxy exercise: it does not yet replace the visibility sector with explicit overlap-defined y_N^{eff} operators in the global scan. The repository now includes three-channel observation fields (`H_to_ee`, `H_to_mumu`, `H_to_tautau`) in `data/pdg_leptons.json` as a reproducible interface for the future overlap-operator migration.

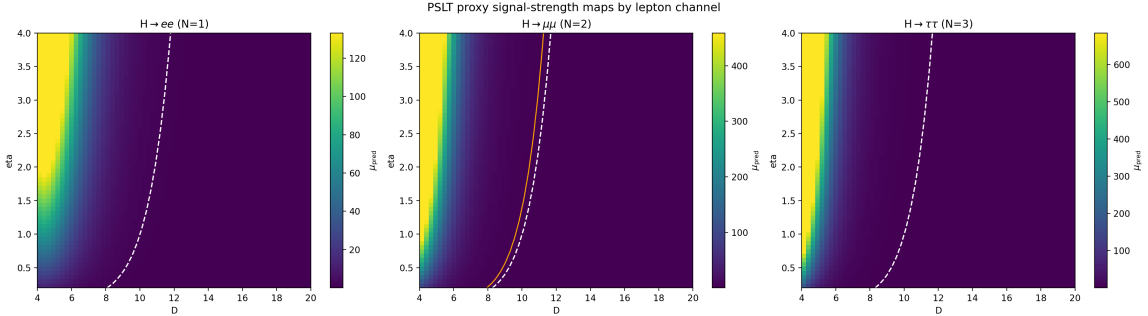


FIG. 8. PSLT proxy extension from $H \rightarrow \mu\mu$ to three lepton channels on the same scan grid: $H \rightarrow ee$ (left), $H \rightarrow \mu\mu$ (middle), and $H \rightarrow \tau\tau$ (right). Each panel shows $\mu_{\ell\ell}^{\text{pred}} = W_N/W_N^{\text{ref}}$ with the same reference point $(D_0, \eta_0) = (10, 1)$.

VIII. DISCUSSION AND CONCLUSION

We have presented a computable EFT-level demonstrator of the Projection Spectral Layer Theory. By closing the loop between geometric inputs and observable layer probabilities, we have shown that:

1. **Generations are spectral:** The “three generation” structure is not an input but a dynamical output of competing entropy (g_N), kinetics (Γ_N), and visibility (B_N).
2. **Stability without ad-hoc cutoffs:** The infinite tower of layers becomes numerically and physically stable once micro-degeneracy is regulated at high N [Eq. (18)] and the observable sector is anchored to the SM Yukawa pattern [Eq. (41)].
3. **Falsifiability:** The closure yields concrete predictions for the winner phase diagram. With D-interpolated $\chi_N^{(LR)}$, the $H \rightarrow \mu\mu$ proxy acceptance forms a restricted band (about 9.4% of the scan), providing a sharper falsifiable constraint on (D, η) .

At the same time, the present implementation keeps three EFT-level surrogates explicit: the Cardy-controlled g_N envelope, the Yukawa-anchored visibility law B_N , and the $H \rightarrow \mu\mu$ proxy map in Eq. (47).

Limitations and outlook. The present closure is internally consistent but remains an EFT-level demonstrator in several places: The use of two parameter sets is a deliberate design choice: action-derived mixing extraction is fixed by Appendix D, while the global (D, η) scan uses a surrogate baseline for map-level robustness.

1. **Observable mapping:** the $H \rightarrow \mu\mu$ comparison uses the proxy $g_{h\mu\mu}^{\text{eff}} \propto \sqrt{W_2}$ rather than a full derivation from the EYMH action. Consistently, the current scan still uses the surrogate visibility law in Eq. (41); the action-derived operator program in Section VI B and Eq. (44) has not yet replaced the global map.
2. **Mixing channel:** under the parity-symmetric first-principles definition [Eq. (50)], we obtain $\chi_N^{(\text{sym})} \sim 10^{-19}$ for $D = \{6, 12, 18\}$ (Appendix C), i.e., symmetry-protected cancellation. We therefore redefine the channel in localized basis, extract $\chi_N^{(LR)}$ (Appendix D), and propagate its D-interpolated profile in the global scan. The remaining gap is a full (D, η, N) localized projection.
3. **Open-system extension:** a Lindblad-type χ_{eff} mechanism is now implemented as a scan-ready diagnostic mode with profiled $\gamma_\phi(D), \gamma_{\text{mix}}(D)$ (Appendix E 3). On $D = 4, \dots, 20$, the diagnostic ratio band is $\chi_{\text{open}}/\chi_{LR} \in [0.0979, 0.1667]$ with unchanged core

map fractions at current resolution; however, the jump operators and rates (L_k, γ_k) are still effective ansatz quantities rather than a microscopic EYMH bath derivation, so this block remains outside baseline figures.

4. **Model-chain unification:** $\chi_N^{(LR)}(D)$ is extracted from the action-derived 2D localized solver (Appendix D), while the global (D, η) scan still uses a simplified kinetic surrogate for rapid mapping. A full end-to-end scan using one identical operator chain for both extraction and phase mapping is left for future work.
5. **Spectral tower:** the baseline validation is strongest for the low-lying bound sector ($N = 1, 2$ in the physical-gap scan), while the high- N contribution is treated at EFT level through (g_N, B_N) regularization.
6. **Finite-time dynamics:** t_{coh} is treated as a control parameter in the baseline scan; a geometry-closed dephasing candidate $t_{\text{coh}}^{(\text{deph})}(D) = \pi/\Delta\omega_{12}(D)$ is benchmarked in Appendix E 5 but is not yet propagated into the reported baseline figures.
7. **Overlap amplitude:** η is scanned as an external control in the baseline maps. A first-principles prefactor candidate $\eta_{\text{fp}}(D)$ from splitting-action data is benchmarked in Appendix E 6; map-level impact is mild in profile-scaled mode but this closure is not yet propagated into baseline figures.
8. **Superradiant channel normalization:** Eq. (32) uses $A_1 = A_2 = 1$ in the baseline maps. An action-derived profile candidate $\tilde{A}_\ell(D)$ is benchmarked in Appendix E 7; it introduces visible map shifts and is therefore kept as diagnostic only.

Status and redefinition of the mixing channel. Using Eq. (33), we fix a basis-independent normalization scale $\bar{\Gamma}_N$ and define the parity-symmetric overlap channel by

$$\begin{aligned} \chi_N^{(\text{sym})}(D) &= \frac{|M_{12}^{(\text{sym})}(D, N)|}{\bar{\Gamma}_N(D)}, \\ M_{12}^{(\text{sym})}(D, N) &= 2\pi \int_0^{\rho_{\max}} \rho d\rho \int_{-z_{\max}}^{z_{\max}} dz \psi_{N,1}^*(\rho, z) \delta V(\rho, z; D) \psi_{N,2}(\rho, z), \end{aligned} \quad (50)$$

and Eq. (38) with the explicit spherical-average δV gives $\chi_N^{(\text{sym})} \approx 0$ (Appendix C). To avoid mixing two inequivalent notions, we redefine the phenomenological mixing channel in a localized-well basis:

$$\psi_{N,L} = \frac{\psi_{N,+} + \psi_{N,-}}{\sqrt{2}}, \quad \psi_{N,R} = \frac{\psi_{N,+} - \psi_{N,-}}{\sqrt{2}}, \quad (51)$$

and define the channel mixing from the corresponding two-state Hamiltonian element:

$$M_{LR}^{(H)}(D, N) \equiv \frac{\lambda_{N,2}(D) - \lambda_{N,1}(D)}{2}, \quad \chi_N^{(LR)}(D) \equiv \frac{|M_{LR}^{(H)}(D, N)|}{\bar{\Gamma}_N(D)}. \quad (52)$$

The baseline mixing entry in Table III is interpreted as the localized-channel coefficient. First-principles localized extraction results are given in Appendix D, and its D-interpolated profile is used in the global (D, η) scan of Section VII. In terminology, $M_{LR}^{(H)}$ is a *closed-system localized-basis splitting* quantity; it is not itself a decoherence rate. Open-system decoherence is introduced separately through Lindblad rates $(\gamma_\phi, \gamma_{\text{mix}})$ in Appendix E 3.

ACKNOWLEDGMENTS

The author acknowledges the use of PDG 2024 data and standard Python scientific stacks for verification.

Appendix A: Action-Derived Chain Reproducibility SOP

This appendix provides a clone-level SOP for reproducing the action-derived extraction chain and the paper-level Fig/Table artifacts.

1. Single Entry Point

From repository root:

```
bash scripts/repro/reproduce_paper.sh
```

Optional modes:

```
bash scripts/repro/reproduce_paper.sh --with-paper
bash scripts/repro/reproduce_paper.sh --package-only
```

2. Step Map and Deliverables

3. Acceptance Conditions

A run is considered reproducible for this manuscript if:

1. the one-click command exits with return code 0;
2. `repro/latest/manifest.json` reports `missing_required = 0`;

TABLE IV. SOP step map for action-derived reproducibility. The one-click wrapper calls these modules in a fixed order and logs each step under `repro/runs/<RUN_ID>/logs/`.

<i>Full per-artifact mapping is listed in <code>repro/artifact_map.csv</code>.</i>		
Stage	Primary scripts	Key outputs
Global maps and proxy plots	<code>generate_plots.py;</code> <code>scan_hll_signal_strengths.py</code>	<code>output/three_generation_*.png;</code> <code>output/hmumu_*.png;</code> <code>output/hll_signal_strength/*</code>
Localized mixing extraction	<code>extract_chi_localized_2d.py</code> (<code>--Ds</code> , <code>--full-scan</code>)	<code>output/chi_fp_2d/localized_chi_D*.csv</code>
Localized-profile diagnostics	<code>diag-chi_profile_robustness.py;</code> <code>plot_chi_*.py</code>	<code>paper/chi_profile_robustness.csv;</code> <code>output/chi_fp_2d/chi_scale_stress_test.csv;</code> <code>paper/chi_wavefunction_contours_D*.png</code>
g_N first-principles candidates	<code>extract_gn_phase_space_candidate.py;</code> <code>gn_phase_space_2d.py;</code> <code>scan_gn_profile_impact.py;</code> <code>scan_gn_nmax_convergence.py;</code> <code>plot_gn_cardy_vs_phase_space.py</code>	<code>output/gn_fp_1d/*.csv; output/gn_fp_2d/*.csv;</code> <code>paper/gn_profile_impact.csv;</code> <code>paper/gn_nmax_convergence.csv;</code> <code>paper/gn_cardy_vs_phase_space.png</code>
Open-system diagnostics	<code>lindblad_chi_minimal.py;</code> <code>extract_chi_open_system_*.py;</code> <code>scan_chi_open_system_*.py</code>	<code>output/chi_open_system/*.csv;</code> <code>paper/chi_open_system_sensitivity.csv</code>
Other first-principles profiles	<code>extract_tcoh_*.py,</code> <code>extract_eta_*.py,</code> <code>extract_superrad_*.py;</code> <code>scan_*_profile_impact.py</code>	<code>paper/tcoh_profile_impact.csv;</code> <code>paper/eta_profile_impact.csv;</code> <code>paper/superrad_profile_impact.csv</code>
Packaging and manifest	<code>package_repro_outputs.py</code> (wrapper <code>repro/runs/<RUN_ID>/figures/</code> ; <code>stage)</code>	<code>repro/runs/<RUN_ID>/tables/;</code> <code>artifact_index.csv;</code> <code>checksums.sha256;</code> <code>manifest.json</code>

3. `repro/latest/checksums.sha256` and `repro/latest/artifact_index.csv` are generated and non-empty.

Appendix B: Action-Derived Effective Potential and WKB

1. Two-Center Harmonic Conformal Factor

We define the conformal factor by a projected Poisson problem on the static slice,

$$\nabla^2 \Omega(\mathbf{x}) = -4\pi a [\rho_\varepsilon(\mathbf{x} - \mathbf{x}_+) + \rho_\varepsilon(\mathbf{x} - \mathbf{x}_-)], \quad \Omega \rightarrow 1 \quad (|\mathbf{x}| \rightarrow \infty), \quad (\text{B1})$$

with $\mathbf{x}_\pm = \pm(D/2)\hat{z}$. Using the Green representation

$$\Omega(\mathbf{x}) = 1 + a \sum_{s=\pm} \int d^3x' \frac{\rho_\varepsilon(\mathbf{x}' - \mathbf{x}_s)}{|\mathbf{x} - \mathbf{x}'|}, \quad (\text{B2})$$

and the normalized Plummer kernel

$$\rho_\varepsilon(\mathbf{r}) = \frac{3\varepsilon^2}{4\pi(|\mathbf{r}|^2 + \varepsilon^2)^{5/2}}, \quad \int d^3r \rho_\varepsilon(\mathbf{r}) = 1, \quad (\text{B3})$$

the integral is analytic and gives

$$\Omega(\rho, z; D) = 1 + a \left(\frac{1}{\sqrt{\rho^2 + (z - D/2)^2 + \varepsilon^2}} + \frac{1}{\sqrt{\rho^2 + (z + D/2)^2 + \varepsilon^2}} \right) \quad (\text{B4})$$

where a is the geometric strength, ε is the core regularization scale, and D is the dual-center separation. Away from the cores ($|\mathbf{x} - \mathbf{x}_\pm| \gg \varepsilon$), this satisfies $\nabla^2\Omega \approx 0$. The radial identity

$$\nabla^2 \left(\frac{1}{\sqrt{r^2 + \varepsilon^2}} \right) = -\frac{3\varepsilon^2}{(r^2 + \varepsilon^2)^{5/2}} \quad (\text{B5})$$

gives the smeared Laplacian:

$$\nabla^2\Omega = -3a\varepsilon^2 \left[(r_+^2 + \varepsilon^2)^{-5/2} + (r_-^2 + \varepsilon^2)^{-5/2} \right] < 0 \quad (\text{B6})$$

which is equivalent to the source form in Eq. (6). This negative contribution is essential for forming the attractive wells in V_{eff} . As a reproducibility check, `verify_omega_geometric_origin.py` confirms $\int d^3r \rho_\varepsilon = 1$ with absolute error 3.75×10^{-7} and validates the radial Laplacian identity with max relative error 1.39×10^{-4} in the non-asymptotic band (see `output/omega_geom_origin/`).

2. \mathbf{V}_{eff} Derivation from KG Equation

Starting from $(\square_g - m_0^2 - \xi R)\Phi = 0$ with $g_{\mu\nu} = \Omega^2 \eta_{\mu\nu}$:

a. *Step 1: \square_g in conformal coordinates.*

$$\square_g \Phi = \Omega^{-2}(-\partial_t^2 + \nabla^2)\Phi + 2\Omega^{-3}\nabla\Omega \cdot \nabla\Phi \quad (\text{B7})$$

b. *Step 2: Time separation.* For $\Phi = e^{-i\omega t}\phi(\mathbf{x})$:

$$\nabla^2\phi + 2\Omega^{-1}\nabla\Omega \cdot \nabla\phi + [\omega^2 - \Omega^2(m_0^2 + \xi R)]\phi = 0 \quad (\text{B8})$$

c. *Step 3: Conformal field rescaling.* Setting $\phi = \Omega^{-1}\psi$ eliminates the first-derivative term. Using $R = -6\Omega^{-3}\nabla^2\Omega$ for 4D conformally flat space:

$[-\nabla^2 + V_{\text{eff}}]\psi = \omega^2\psi, \quad V_{\text{eff}} = m_0^2\Omega^2 + (1 - 6\xi)\Omega^{-1}\nabla^2\Omega$

(B9)

d. *Double-well formation condition.* For $\xi < 1/6$ and $\nabla^2\Omega < 0$ near cores, the curvature term contributes **negatively** to V_{eff} , creating attractive wells. The mass term $m_0^2\Omega^2$ provides the continuum threshold at infinity.

e. *Self-consistency check.* At $\xi = \xi_c = 1/6$ (conformal coupling): $V_{\text{eff}} \rightarrow m_0^2 \Omega^2$, and the curvature contribution vanishes identically. ✓

3. 1D On-Axis Reduction

For efficient scanning, we use the on-axis ($\rho = 0$) reduction:

$$\left[-\frac{d^2}{dz^2} + U(z) \right] \psi_n(z) = E_n \psi_n(z), \quad U(z) = V_{\text{eff}}(\rho = 0, z) - m_0^2 \quad (\text{B10})$$

where $E_n = \omega_n^2 - m_0^2$. Bound states satisfy $E_n < 0$; stable modes additionally require $\omega_n^2 = m_0^2 + E_n > 0$.

4. 2D Axisymmetric Validation

We validated the 1D reduction by comparing with the full 2D axisymmetric Laplacian:

$$\nabla^2 \Omega = \frac{\partial^2 \Omega}{\partial \rho^2} + \frac{1}{\rho} \frac{\partial \Omega}{\partial \rho} + \frac{\partial^2 \Omega}{\partial z^2} \quad (\text{B11})$$

For the physical-gap parameters ($a = 0.04$, $\varepsilon = 0.1$, $m_0 = 1$, $\xi = 0.14$), the relative error at $\rho = 0$ is:

D	Max $ U_{2D} - U_{1D} / \max U $
6	4.0×10^{-4}
12	4.0×10^{-4}
18	4.0×10^{-4}

The 1D 3D-identity approximation is accurate to $< 0.1\%$, validating its use for phase scans.

5. WKB Action Convention

The tunneling action through the central barrier is:

$$S_N = \int_{z_1}^{z_2} \sqrt{U(z) - E_N} dz \quad (\text{B12})$$

where $z_{1,2}$ are the turning points satisfying $U(z_{1,2}) = E_N$. The tunneling suppression factor is:

$$r_N = \eta \cdot e^{-2S_N} \quad (\text{B13})$$

Convention note: For rates/probabilities we use e^{-2S} , while the level-splitting amplitude scales as e^{-S} . The empirical splitting relation below therefore tests the amplitude-level law.

6. Splitting–Action Consistency Check

The most stringent internal consistency check is the relation between level splitting and tunneling action. For symmetric double wells, WKB theory predicts $\Delta E \propto e^{-S}$. From our action-derived scan:

$$\ln \Delta E \approx -1.01 S_1 + 0.69, \quad R^2 = 0.9999 \quad (\text{B14})$$

This near-perfect linear relation (Fig. 9) confirms that the **same** V_{eff} controls both the spectrum and the tunneling kinetics—not an engineered coincidence.

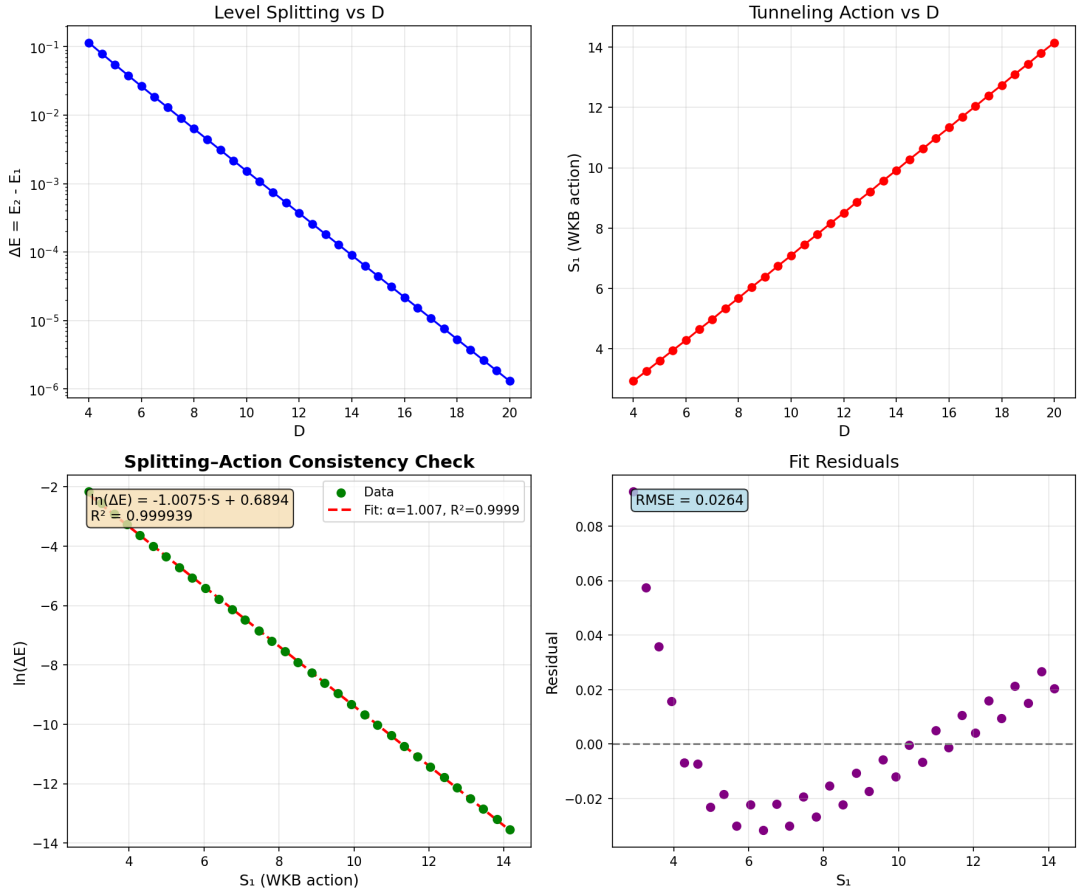


FIG. 9. Splitting–action consistency check. The level splitting $\Delta E = E_2 - E_1$ follows $\exp(-S_1)$ to $R^2 = 0.9999$, confirming the action-derived V_{eff} governs both spectrum and tunneling.

7. Action-Derived Numerical Results

Table V shows the key spectral and tunneling quantities from the action-derived calculation. Grid convergence: $|E_1|$ variation < 0.2% for $dz \in [0.01, 0.02]$ at fixed $z_{\text{max}} = 80$.

TABLE V. Action-derived spectral and tunneling data. Parameters: $a = 0.04$, $\varepsilon = 0.1$, $m_0 = 1$, $\xi = 0.14$.

D	E_1	E_2	ω_1	S_1	ΔE
4	-0.505	-0.390	0.704	2.92	1.15×10^{-1}
8	-0.476	-0.469	0.724	5.68	6.32×10^{-3}
12	-0.478	-0.478	0.722	8.51	3.69×10^{-4}
16	-0.481	-0.481	0.721	11.33	2.19×10^{-5}
20	-0.482	-0.482	0.720	14.16	1.30×10^{-6}

8. Bound-State omega Convergence Benchmark

To make the surrogate-vs-exact distinction explicit, we report a direct bound-state benchmark for ω_N from the same action-derived 1D operator chain used in Table V. The settings are fixed to the physical-gap parameter set ($a = 0.04$, $\varepsilon = 0.1$, $m_0 = 1$, $\xi = 0.14$), $z_{\max} = 80$, and three resolutions: coarse ($N_z = 4001$), mid ($N_z = 6001$), fine ($N_z = 8001$). The reproducible script is `code/extract_omega_exact_convergence.py`.

TABLE VI. Bound-state ω_N convergence benchmark at $D = \{6, 12, 18\}$ from the action-derived operator chain. Relative errors are quoted versus fine grid.

D	level	N_z	ω_1	ω_2	$\Delta\omega_{12}$	max rel. ω vs fine
6	coarse	4001	0.720883	0.738989	1.8107×10^{-2}	8.65×10^{-4}
6	mid	6001	0.721345	0.739468	1.8123×10^{-2}	2.18×10^{-4}
6	fine	8001	0.721500	0.739629	1.8129×10^{-2}	0
12	coarse	4001	0.721781	0.722035	2.5438×10^{-4}	8.84×10^{-4}
12	mid	6001	0.722258	0.722513	2.5533×10^{-4}	2.23×10^{-4}
12	fine	8001	0.722418	0.722674	2.5565×10^{-4}	0
18	coarse	4001	0.719404	0.719408	3.6700×10^{-6}	8.92×10^{-4}
18	mid	6001	0.719885	0.719888	3.6943×10^{-6}	2.25×10^{-4}
18	fine	8001	0.720046	0.720050	3.7025×10^{-6}	0

This benchmark is the operator-level reference for ω_N in the bound-state convention. In contrast, Appendix D uses generalized localized-extraction eigenvalues λ for mixing-channel extraction; the two quantities serve different roles and are not identified.

9. Fixed-dz Convergence

We verified numerical stability using fixed grid spacing dz (rather than fixed N_z):

- For $dz \in \{0.04, 0.02, 0.01\}$ and $z_{\max} \in \{60, 80\}$: E_1 variation $< 0.3\%$, S_1 variation $< 0.2\%$.

- Results are independent of z_{\max} for $z_{\max} > 60$ (domain truncation error negligible).

Appendix C: First-Principles Symmetry-Channel Test for chi

Using the explicit definition in Eq. (50), we computed M_{12} and $\chi_N^{(\text{sym})}$ on 2D axisymmetric grids for $D = \{6, 12, 18\}$ with coarse/mid/fine resolutions. The modes are normalized with the cylindrical measure $2\pi\rho d\rho dz$, and orthogonality satisfies $|\langle\psi_1, \psi_2\rangle| < 10^{-15}$ in all runs.

TABLE VII. Fine-grid symmetry-channel extraction using Eq. (50). Parameters: $a = 0.04$, $\varepsilon = 0.1$, $m_0 = 1$, $\xi = 0.14$.

D	$ M_{12}^{(\text{sym})} $	$\chi_N^{(\text{sym})}$	$ \langle\psi_1, \psi_2\rangle $
6	2.09×10^{-16}	1.66×10^{-19}	3.12×10^{-17}
12	6.03×10^{-16}	5.69×10^{-19}	3.47×10^{-18}
18	6.24×10^{-16}	6.20×10^{-19}	2.11×10^{-16}

These values are numerically consistent with symmetry-protected cancellation of the parity-symmetric overlap channel. Across coarse/mid/fine grids, $M_{12}^{(\text{sym})}$ changes sign but remains at $\mathcal{O}(10^{-16})$, indicating no resolved nonzero mixing in this channel.

For this reason, the phenomenological Rank-2 coefficient in the main text is interpreted as a localized-channel effective coupling (Section VIII), not as $\chi_N^{(\text{sym})}$ from Eq. (50).

Appendix D: Localized-Channel First-Principles Extraction of chi

We compute the nonzero mixing channel directly in localized basis using

$$M_{LR}^{(H)} = \frac{\lambda_2 - \lambda_1}{2}, \quad \chi_N^{(LR)} = \frac{|M_{LR}^{(H)}|}{\bar{\Gamma}_N}, \quad (\text{D1})$$

with $\bar{\Gamma}_N$ from Eq. (33). Here $\lambda_{1,2}$ are generalized operator eigenvalues from $K\psi = \lambda M\psi$ in the localized extraction solver; they are not the bound-state energy convention $E = \omega^2 - m_0^2 < 0$ used in Appendix B. The extraction uses `code/extract_chi_localized_2d.py` with fixed settings:

- Domain: $\rho_{\max} = 3.0$, $z_{\max} = D/2 + 6.0$.
- Grids: coarse $(d\rho, dz) = (0.12, 0.06)$, mid $(0.08, 0.04)$, fine $(0.06, 0.03)$.
- Solver: generalized eigensystem (shift-invert low-mode targeting, $\sigma = 2.5$), tolerance 10^{-8} , maxiter 3×10^4 .
- Acceptance criteria: $\delta_{\Delta E} \equiv |\Delta E_{\text{level}} - \Delta E_{\text{fine}}| / |\Delta E_{\text{fine}}| < 5\%$, $\delta_\chi \equiv |\chi_{\text{level}} - \chi_{\text{fine}}| / |\chi_{\text{fine}}| < 5\%$, and null-channel absolute bound $|M_{12}^{(\text{sym})}| < 10^{-12}$.

TABLE VIII. Localized-channel extraction for $D = \{6, 12, 18\}$ (coarse/mid/fine). Parameters: $a = 0.04$, $\varepsilon = 0.1$, $m_0 = 1$, $\xi = 0.14$.

D	level	$(d\rho, dz)$	(N_ρ, N_z)	λ_1	λ_2	$M_{LR}^{(H)}$	$\chi_N^{(LR)}$	$ M_{12}^{(\text{sym})} $
6	coarse	(0.12, 0.06)	(25, 300)	2.14765	2.60073	2.26541×10^{-1}	4.13261×10^{-4}	5.29×10^{-17}
6	mid	(0.08, 0.04)	(38, 450)	2.14362	2.59798	2.27178×10^{-1}	4.17350×10^{-4}	2.44×10^{-19}
6	fine	(0.06, 0.03)	(50, 600)	2.16611	2.62106	2.27474×10^{-1}	4.01827×10^{-4}	1.56×10^{-18}
12	coarse	(0.12, 0.06)	(25, 400)	2.36032	2.71730	1.78492×10^{-1}	2.27261×10^{-4}	2.89×10^{-17}
12	mid	(0.08, 0.04)	(38, 600)	2.35598	2.71374	1.78883×10^{-1}	2.29384×10^{-4}	6.96×10^{-17}
12	fine	(0.06, 0.03)	(50, 800)	2.37821	2.73632	1.79054×10^{-1}	2.21414×10^{-4}	1.03×10^{-17}
18	coarse	(0.12, 0.06)	(25, 500)	2.22204	2.49466	1.36311×10^{-1}	2.18683×10^{-4}	1.94×10^{-17}
18	mid	(0.08, 0.04)	(38, 750)	2.21686	2.49001	1.36575×10^{-1}	2.21053×10^{-4}	1.54×10^{-15}
18	fine	(0.06, 0.03)	(50, 1000)	2.23864	2.51202	1.36694×10^{-1}	2.13187×10^{-4}	2.19×10^{-16}

The complete pipeline, scripts, and raw tables used here are available in the project repository: <https://github.com/boypatrick/PSLT>.

Across all non-fine runs in Table VIII, we obtain

$$\max \delta_{\Delta E} = 4.10 \times 10^{-3}, \quad \max \delta_\chi = 3.86 \times 10^{-2}, \quad \max |M_{12}^{(\text{sym})}| = 1.54 \times 10^{-15}, \quad (\text{D2})$$

which satisfies the stated convergence and absolute-null criteria.

For interpolation support and reproducibility of scan-level diagnostics, we additionally ran a fine-grid-only auxiliary sweep on integer separations $D = 4, \dots, 20$ using the same solver settings (`--full-scan` in `extract_chi_localized_2d.py`). These points are used as profile-support data in the repository, while the formal acceptance criteria above remain defined by the benchmark convergence set $D = \{6, 12, 18\}$.

Figure 10 shows the fine-grid 2D parity eigenmodes used in the localized extraction at $D = \{6, 12, 18\}$. The expected even/odd nodal structure is manifest and remains stable across the three benchmark separations.

To test profile uncertainty in the global map, we benchmarked six $\chi_N^{(LR)}(D)$ choices built from the same fine-grid knots $(D, \chi_N^{(LR)}) = \{(6, 4.02 \times 10^{-4}), (12, 2.21 \times 10^{-4}), (18, 2.13 \times 10^{-4})\}$: linear interpolation, log-linear exponential fit $\ln \chi = -7.5956 - 0.05282 D$, and $\pm 20\%$ amplitude rescalings of each profile. Re-running the full 60×60 scan gives identical grid-level summary metrics (within scan resolution):

$$f(\mathcal{R}_3 > 0.90) = 0.800, \quad f(\mathcal{R}_3 > 0.95) = 0, \quad f(\chi_{\mu\mu}^2 < 4) = 0.094, \quad (\text{D3})$$

with the same best-fit point $(D, \eta) \approx (9.97, 1.36)$. Thus, at current scan resolution, profile-interpolation uncertainty is subdominant to other model-systematics.

TABLE IX. Auxiliary fine-grid localized profile points from the full-scan run ($D = 4\text{--}20$). Source CSV: `output/chi_fp_2d/localized_chi_D4-5-...-20.csv`.

D	λ_1	λ_2	$\chi_N^{(LR)}$
4	2.06671	2.56696	5.266×10^{-4}
5	2.34635	2.85471	3.311×10^{-4}
6	2.16611	2.62106	4.018×10^{-4}
7	2.42273	2.88524	2.661×10^{-4}
8	2.24778	2.66479	3.202×10^{-4}
9	2.10111	2.48071	3.758×10^{-4}
10	2.32055	2.70644	2.623×10^{-4}
11	2.17620	2.52926	3.064×10^{-4}
12	2.37821	2.73632	2.214×10^{-4}
13	2.24440	2.57510	2.554×10^{-4}
14	2.42772	2.76173	1.906×10^{-4}
15	2.30010	2.61030	2.181×10^{-4}
16	2.47457	2.78817	1.661×10^{-4}
17	2.34884	2.64089	1.895×10^{-4}
18	2.23864	2.51202	2.132×10^{-4}
19	2.39519	2.67161	1.663×10^{-4}
20	2.28581	2.54509	1.867×10^{-4}

TABLE X. Extended profile-sensitivity test for $\chi_N^{(LR)}(D)$ in the 60×60 global scan. Source data file: `paper/chi_profile_robustness.csv`.

Profile	$f(\mathcal{R}_3 > 0.90)$	$f(\mathcal{R}_3 > 0.95)$	$f(\chi_{\mu\mu}^2 < 4)$	Best (D, η)
Linear interpolation	0.800	0	0.094	(9.97, 1.36)
Exponential fit	0.800	0	0.094	(9.97, 1.36)
Linear $\times 0.8$	0.800	0	0.094	(9.97, 1.36)
Linear $\times 1.2$	0.800	0	0.094	(9.97, 1.36)
Exp-fit $\times 0.8$	0.800	0	0.094	(9.97, 1.36)
Exp-fit $\times 1.2$	0.800	0	0.094	(9.97, 1.36)

As a stronger stress test, we further rescaled the localized profile by large factors and tracked boundary movement directly on the (D, η) grid. Figure 11 shows that the user-requested cases $\times 0.5$ and $\times 2$ remain exactly coincident with baseline boundaries at this scan resolution. In this setup, the first visible boundary drift appears only in the $H \rightarrow \mu\mu$ proxy mask near $\times 10^5$, while the $\mathcal{R}_3 > 0.90$ boundary remains unchanged throughout the tested range. All boundary-coincidence statements in this paragraph refer to the present 60×60 scan resolution.

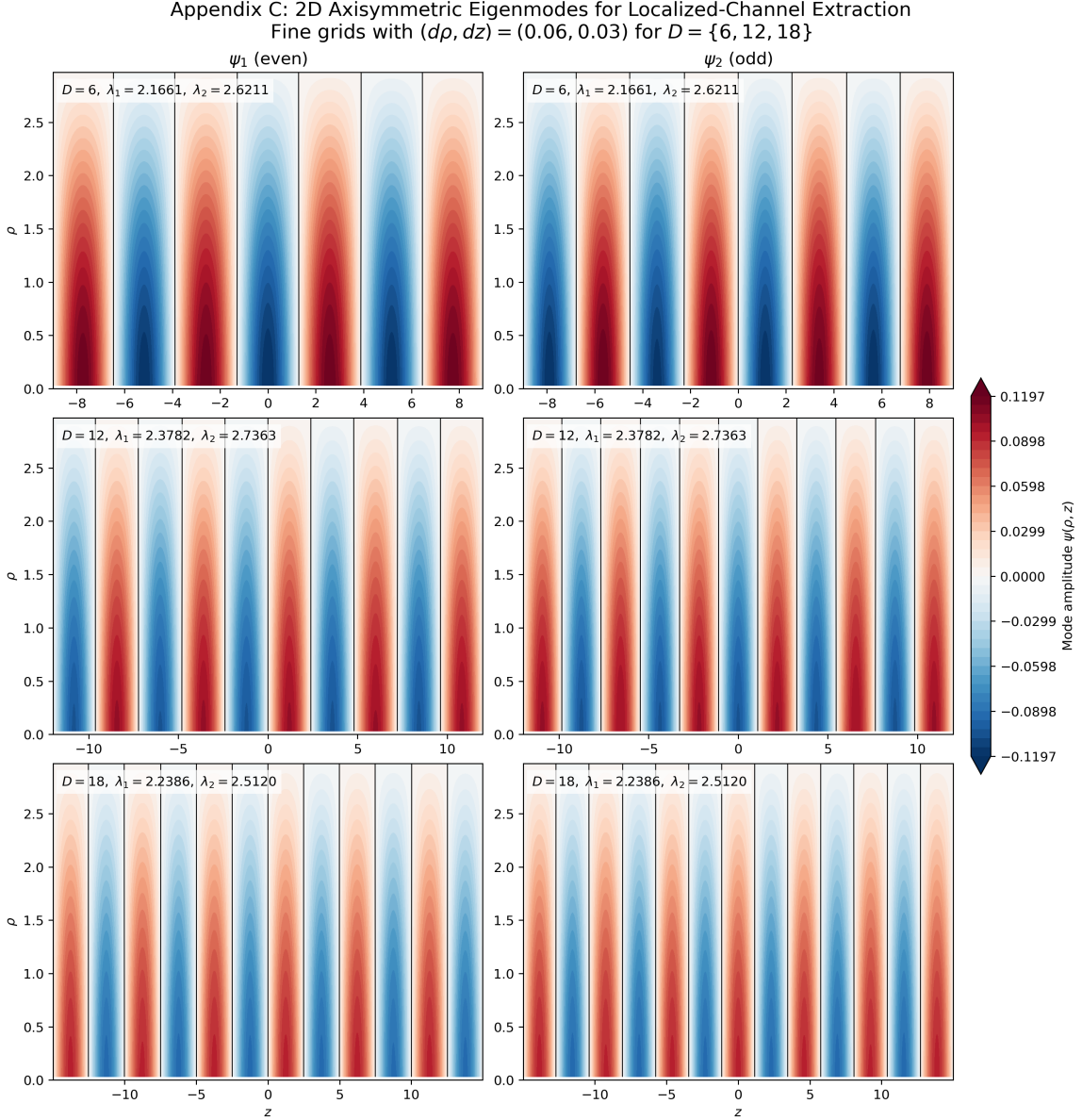


FIG. 10. Fine-grid 2D axisymmetric eigenmodes used in Appendix D. Each row corresponds to one benchmark separation ($D = 6, 12, 18$); columns show the lowest even/odd parity modes (ψ_1, ψ_2) entering the localized-channel extraction pipeline.

Appendix E: Preliminary First-Principles Replacement Candidate Checks

1. 1D Phase-Space Candidate for g_N

To test a first-principles replacement direction for Eq. (18), we evaluated the semiclassical 1D candidate on the same action-derived axis potential:

$$\rho_{\text{WKB}}(E; D) = \frac{1}{2\pi} \int_{U(z; D) < E} \frac{dz}{\sqrt{E - U(z; D)}}, \quad (\text{E1})$$

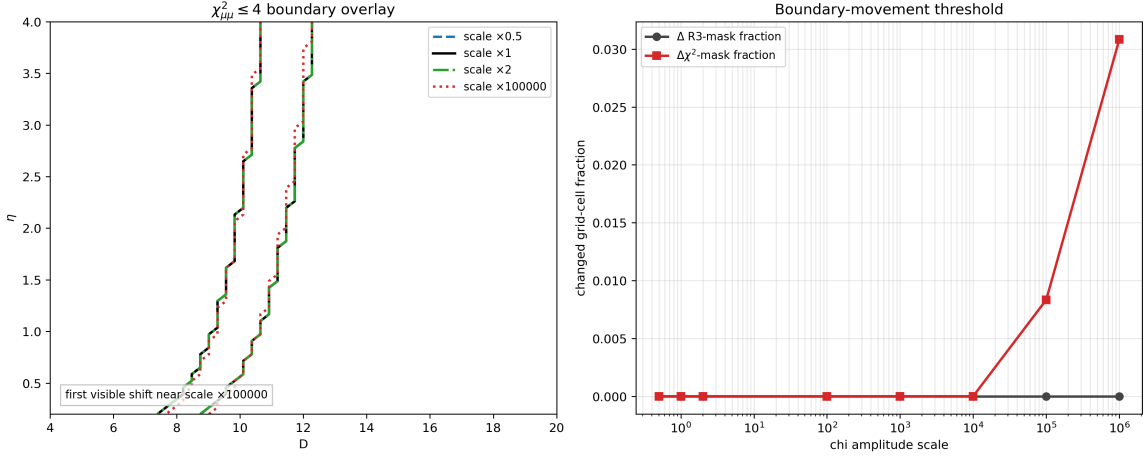


FIG. 11. Strong χ -amplitude stress test on the global map. Left: overlay of $\chi_{\mu\mu}^2 \leq 4$ boundary for selected scales, including the requested $\times 0.5$ and $\times 2$, plus an extreme scale where drift first appears. Right: changed-cell fractions versus scale (relative to baseline $\times 1$). Source data file: `output/chi_fp_2d/chi_scale_stress_test.csv`.

TABLE XI. Preliminary 1D phase-space candidate $g_N^{(\text{ps})}$ at $D = 12$. Source CSV: `output/gn_fp_1d/gn_phase_space_candidate_D12.csv`.

level	dz	E_1	E_2	E_3	$g_1^{(\text{ps})}$	$g_2^{(\text{ps})}$	max rel.g vs fine
coarse	0.04	-0.636696	-0.608074	-0.575010	1.056725	1.054421	1.31×10^{-2}
mid	0.02	-0.637061	-0.608419	-0.575335	1.066813	1.074099	5.30×10^{-3}
fine	0.01	-0.637233	-0.608582	-0.575488	1.063919	1.068433	0

$$g_N^{(\text{ps})}(D) = 1 + \int_{E_{\min}(D)}^{E_N(D)} \rho_{\text{WKB}}(E'; D) dE', \quad E_{\min}(D) \equiv \min_z U(z; D). \quad (\text{E2})$$

Using the reproducible script `extract_gn_phase_space_candidate.py` (in the `code/` directory), we ran a coarse/mid/fine test at $D = 12$ (Table XI). The candidate is numerically stable at the few- 10^{-3} level versus fine grid.

2. 2D Axisymmetric Benchmark for $g_N^{(\text{ps})}$

To reduce projection ambiguity, we also ran a 2D axisymmetric benchmark on $D = \{6, 12, 18\}$ using the same localized extraction chain as Appendix D: identical generalized operator build, identical box/range convention, and the same shift-invert low-mode settings ($\sigma = 2.5$, $\text{tol} = 10^{-8}$, $\text{maxiter} = 3 \times 10^4$). We define

$$N_{\text{ps}}(E) = \frac{1}{4\pi} \int d^2x d^2p \Theta(E - U - p^2) = \frac{1}{2} \int \rho d\rho dz [E - U(\rho, z)]_+, \quad (\text{E3})$$

TABLE XII. Fine-grid 2D phase-space profile candidate at $D = \{6, 12, 18\}$. Source CSV: `output/gn_fp_2d/gn_phase_space_2d_D6-12-18.csv`.

D	λ_1	λ_2	λ_3	\hat{g}_1	\hat{g}_2
6	0.719476	0.804126	0.945018	9.867×10^{-2}	4.370×10^{-1}
12	0.686186	0.747510	0.822830	1.193×10^{-1}	5.146×10^{-1}
18	0.667848	0.713807	0.767832	1.291×10^{-1}	5.294×10^{-1}

Low- N comparison: Cardy baseline vs 2D phase-space profile

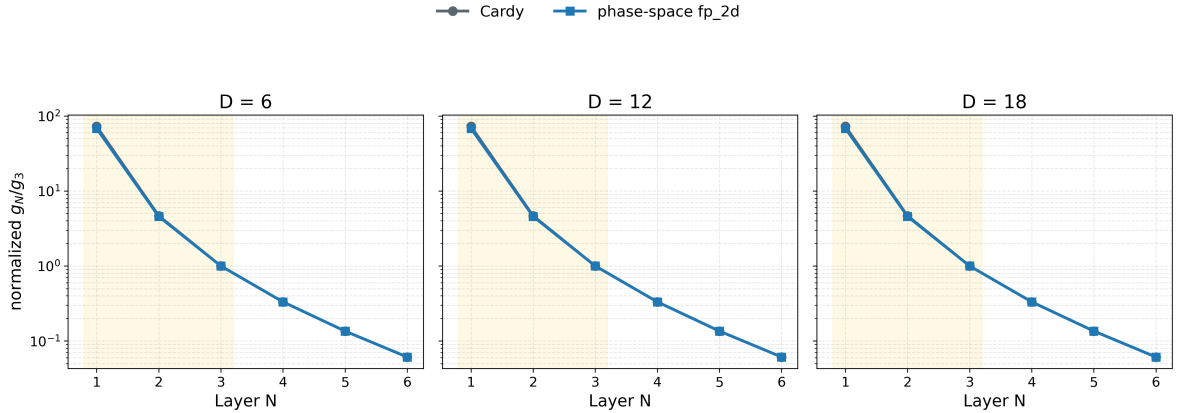


FIG. 12. Low- N comparison between Cardy baseline and 2D phase-space profile on $D = \{6, 12, 18\}$, shown as normalized ratios g_N/g_3 (log scale). The highlighted band marks $N = 1, 2, 3$. Source files: `paper/gn_cardy_vs_phase_space.png`, `paper/gn_cardy_vs_phase_space.csv`.

$$\mathcal{W}_N \equiv [\lambda_1, \lambda_N], \quad g_{N,\text{raw}}^{(\text{ps})} = 1 + \int_{\mathcal{W}_N} \rho_{\text{ps}}(E') dE' = 1 + N_{\text{ps}}(\lambda_N) - N_{\text{ps}}(\lambda_1), \quad \hat{g}_N \equiv \frac{g_{N,\text{raw}}^{(\text{ps})}}{g_{3,\text{raw}}^{(\text{ps})}}. \quad (\text{E4})$$

The script `extract_gn_phase_space_2d.py` (in `code/`) exports both the low- N profile table and the low-mode spectral table with explicit window bounds (source CSVs: `output/gn_fp_2d/gn_phase_space_2d.csv`, `output/gn_fp_2d/gn_phase_space_2d_spectrum_D6-12-18.csv`). For non-fine levels, the maximum profile deviation is

$$\max_{\text{non-fine}} \left(\max_N \frac{|\hat{g}_N - \hat{g}_N^{(\text{fine})}|}{|\hat{g}_N^{(\text{fine})}|} \right) = 2.35 \times 10^{-2}. \quad (\text{E5})$$

As in the 1D candidate check, this benchmark is reported as a replacement candidate. To test map-level impact, we connected both candidates to the main scan through `g_mode` choices (`cardy`, `fp_1d`, `fp_2d`) and the reproducible script `scan_gn_profile_impact.py`. Results in Table XIII show that the main conclusion is retained: $f(\mathcal{R}_3 > 0.90)$ shifts by at most 0.0167 (absolute), while high- N runaway remains controlled with $f(N_{\text{win}} > 3) = 0$ in all tested modes.

Across $N_{\text{max}} = 20, 30, 40$, both baseline and `fp_2d` scenarios are numerically stable at map level: the key fractions $f(\mathcal{R}_3 > 0.90)$, $f(\chi^2_{\mu\mu} < 4)$, and $f(N_{\text{win}} > 3)$ remain unchanged in this

TABLE XIII. Map-level impact of first-principles g_N profiles on the 60×60 scan (diagnostic only; baseline remains Cardy mode). Source CSV: `paper/gn_profile_impact.csv`.

case	$f(\mathcal{R}_3 > 0.90)$	$f(\chi_{\mu\mu}^2 < 4)$	$f(N_{\text{win}} > 3)$	mean tail prob.
baseline Cardy	0.800	0.0942	0.000	0.0873
g_N fp_1d profile	0.800	0.0942	0.000	0.0894
g_N fp_2d profile	0.783	0.0942	0.000	0.0905

TABLE XIV. N_{max} convergence check for baseline and g_N fp_2d map-level summaries. Source CSV: `paper/gn_nmax_convergence.csv`.

case	N_{max}	$f(\mathcal{R}_3 > 0.90)$	$f(\chi_{\mu\mu}^2 < 4)$	$f(N_{\text{win}} > 3)$	mean tail prob.
baseline Cardy	20	0.800	0.0942	0.000	0.087284
baseline Cardy	30	0.800	0.0942	0.000	0.087284
baseline Cardy	40	0.800	0.0942	0.000	0.087284
g_N fp_2d profile	20	0.783	0.0942	0.000	0.090492
g_N fp_2d profile	30	0.783	0.0942	0.000	0.090492
g_N fp_2d profile	40	0.783	0.0942	0.000	0.090492

scan.

3. Geometry-Informed Lindblad Scan-Ready Module for Open-System χ

As a methodological bridge (not a replacement of Appendix D), we consider a two-level open-system model in the standard GKSL/Lindblad form [10, 11]:

$$\dot{\rho} = -i[H, \rho] + \gamma_\phi \mathcal{D}[\sigma_z]\rho + \gamma_{\text{mix}} \mathcal{D}[\sigma_x]\rho, \quad H = \begin{pmatrix} 0 & \Delta/2 \\ \Delta/2 & 0 \end{pmatrix}. \quad (\text{E6})$$

As external motivation for this diagnostic direction, recent entanglement-based flavor analyses report that minimizing scattering-generated entanglement can qualitatively reproduce observed CKM/PMNS patterns [12]. In this manuscript we use that connection only as qualitative support for coherence-sensitive diagnostics, not as a baseline closure assumption. For this module we set $\gamma_{\text{mix}}(D) \equiv M_{LR}^{(H)}(D)$ from Appendix D, and define a geometry-informed dephasing proxy

$$\gamma_\phi(D) \equiv \sqrt{\langle (\delta V)^2 \rangle_\rho}, \quad \delta V = V_{\text{eff}} - \bar{V}_{\text{eff}}(r), \quad (\text{E7})$$

with cylindrical weighting $\langle \dots \rangle_\rho$. The minimal Lindblad evolution is generated by `lindblad_chi_minimal.py`, and geometry-profile extraction is handled by `extract_chi_open_system_geometry.py`. These scripts output reproducible diagnostics such as

$$C_{\text{max}} \equiv \max_t |\rho_{LR}(t)|, \quad P_{\text{max}} \equiv \max_t \rho_{RR}(t), \quad (\text{E8})$$

TABLE XV. Geometry-informed open-system demonstrator at $D = \{6, 12, 18\}$. Source CSV: `output/chi_open_system/chi_open_system_geometry_D6-12-18.csv`.

D	γ_ϕ	γ_{mix}	C_{max}	$\chi_{\text{eff}}^{(\text{proxy})}$	$\chi_N^{(LR)}$	ratio
6	0.656901	0.227474	0.077658	6.24×10^{-5}	4.02×10^{-4}	0.155
12	0.744389	0.179054	0.063765	2.82×10^{-5}	2.21×10^{-4}	0.128
18	0.805854	0.136694	0.051381	2.19×10^{-5}	2.13×10^{-4}	0.103

TABLE XVI. Open-system sensitivity scan with profiled $(\gamma_\phi, \gamma_{\text{mix}})$ on the 60×60 map. Source CSV: `paper/chi_open_system_sensitivity.csv`.

case	ratio min	ratio max	ratio mean
baseline localized	1.000	1.000	1.000
open-system base (1, 1)	0.097	0.160	0.124
$\phi \times 0.5$, mix $\times 1$	0.146	0.216	0.178
$\phi \times 2$, mix $\times 1$	0.059	0.115	0.082
$\phi \times 1$, mix $\times 0.5$	0.058	0.109	0.079
$\phi \times 1$, mix $\times 2$	0.148	0.228	0.184
$\phi \times 0.5$, mix $\times 2$	0.206	0.275	0.232
$\phi \times 2$, mix $\times 0.5$	0.032	0.068	0.046

and a normalized proxy $\chi_{\text{eff}}^{(\text{proxy})} = 2\gamma_{\text{mix}}C_{\text{max}}/\bar{\Gamma}_N$. Results for $D = \{6, 12, 18\}$ are summarized in Table XV. Extending the same profile to $D = 4, \dots, 20$ gives a stable baseline ratio band $\chi_{\text{open}}/\chi_{LR} \in [0.0979, 0.1667]$ with mean 0.1290 (source CSV: `output/chi_open_system/chi_open_ratio_band.csv`).

Across all sensitivity cases in Table XVI, the core scan summaries remain unchanged on this grid: $f(\mathcal{R}_3 > 0.90) = 0.800$, $f(\mathcal{R}_3 > 0.95) = 0$, $f(\chi_{\mu\mu}^2 < 4) = 0.0942$, and $f(N_{\text{win}} > 3) = 0$. These values are model-dependent because the Lindblad structure is still an effective environment ansatz and not yet a microscopic EYMH bath derivation; therefore, `chi_mode=open_system` is treated as scan-ready diagnostic only and is not propagated into baseline reported figures.

4. Cross-Module Migration Snapshot

To compare the two main first-principles migration directions on the same map-level metrics, we aggregate three scenarios: baseline (`cardy + localized`), g_N profile replacement (`fp_2d + localized`), and open-system χ (`cardy + open_system`). The reproducible script is `scan_first_principles_migration_summary.py`; outputs are `paper/first_principles_migration_summary.csv` and Fig. 13.

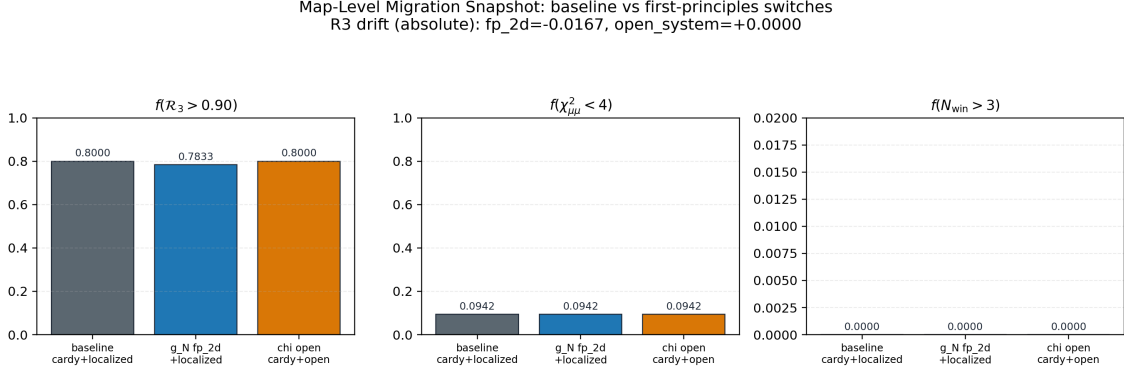


FIG. 13. Map-level migration snapshot across three scenarios. Left to right: $f(\mathcal{R}_3 > 0.90)$, $f(\chi_{\mu\mu}^2 < 4)$, and $f(N_{\text{win}} > 3)$.

TABLE XVII. Cross-module migration comparison from `paper/first_principles_migration_summary.csv`.

scenario	$f(\mathcal{R}_3 > 0.90)$	$\Delta f(\mathcal{R}_3 > 0.90)$	$f(\chi_{\mu\mu}^2 < 4)$	$f(N_{\text{win}} > 3)$
baseline (cardy + localized)	0.800	0.0000	0.0942	0.0000
g_N migration (<code>fp_2d + localized</code>)	0.783	-0.0167	0.0942	0.0000
χ migration (<code>cardy + open_system</code>)	0.800	0.0000	0.0942	0.0000

5. Dephasing-Based First-Principles Candidate for t_{coh}

To close the finite-time module with the same action-derived spectral chain, we test the dephasing candidate

$$\Delta\omega_{12}(D) \equiv \omega_2(D) - \omega_1(D), \quad t_{\text{coh}}^{(\text{deph})}(D) \equiv \frac{\pi}{\Delta\omega_{12}(D)}, \quad (\text{E9})$$

where (ω_1, ω_2) are extracted from the bound-state convention $E_n = \omega_n^2 - m_0^2 < 0$ in the same 1D on-axis operator chain as Appendix B. The reproducible implementation is provided in the code directory (`extract_tcoh_dephasing_1d.py`).

For non-fine levels, the maximum relative deviation is

$$\max\left(\frac{|t_{\text{coh}} - t_{\text{coh}}^{(\text{fine})}|}{|t_{\text{coh}}^{(\text{fine})}|}\right) = 8.86 \times 10^{-3}, \quad (\text{E10})$$

which is numerically stable at the sub- 10^{-2} level for this benchmark set.

To assess map-level impact, we compared three cases on the same 60×60 (D, η) grid: baseline constant $t_{\text{coh}} = 1$, raw dephasing profile from Eq. (E9), and a capped variant $\min(t_{\text{coh}}^{(\text{deph})}, 10^4)$. Results are summarized in Table XIX (source CSV: `paper/tcoh_profile_impact.csv`).

The dephasing candidate leaves \mathcal{R}_3 summary fractions unchanged on this grid, but significantly alters the proxy-compatible $H \rightarrow \mu\mu$ area. Therefore, in this manuscript, Eq. (E9) is

TABLE XVIII. 1D on-axis dephasing candidate for t_{coh} at $D = \{6, 12, 18\}$ (coarse/mid/fine). Source CSV: `output/tcoh_fp_1d/tcoh_dephasing_D6-12-18.csv`.

D	level	ω_1	ω_2	$\Delta\omega_{12}$	$t_{\text{coh}}^{(\text{deph})}$
6	coarse	0.720883	0.738989	1.8107×10^{-2}	1.7350×10^2
6	mid	0.721345	0.739468	1.8123×10^{-2}	1.7334×10^2
6	fine	0.721500	0.739629	1.8129×10^{-2}	1.7329×10^2
12	coarse	0.721781	0.722035	2.5438×10^{-4}	1.2350×10^4
12	mid	0.722258	0.722513	2.5533×10^{-4}	1.2304×10^4
12	fine	0.722418	0.722674	2.5565×10^{-4}	1.2289×10^4
18	coarse	0.719404	0.719408	3.6700×10^{-6}	8.5602×10^5
18	mid	0.719885	0.719888	3.6943×10^{-6}	8.5039×10^5
18	fine	0.720046	0.720050	3.7025×10^{-6}	8.4850×10^5

TABLE XIX. Global-scan impact of the dephasing t_{coh} candidate (diagnostic only; not baseline).

case	$f(\mathcal{R}_3 > 0.90)$	$f(\mathcal{R}_3 > 0.95)$	$f(\chi_{\mu\mu}^2 < 4)$	best χ^2
constant $t_{\text{coh}} = 1$	0.800	0.000	0.094	3.05×10^{-7}
$\pi/\Delta\omega_{12}(D)$	0.800	0.000	0.344	2.46×10^{-5}
$\min(\pi/\Delta\omega_{12}, 10^4)$	0.800	0.000	0.188	2.46×10^{-5}

reported as a first-principles candidate benchmark only and is not propagated into the baseline reported figures.

6. Splitting-Prefactor First-Principles Candidate for η

To test a geometry-closed replacement direction for the overlap amplitude in Eq. (24), we use the same action-derived quantities ($\Delta E_{12}, S_1$) and define the splitting prefactor

$$\Delta E_{12}(D) \approx A_{12}(D) e^{-S_1(D)}, \quad A_{12}(D) \equiv \Delta E_{12}(D) e^{S_1(D)}. \quad (\text{E11})$$

With a reference point $D_{\text{ref}} = 12$, we define two dimensionless candidates:

$$\eta_{\text{amp}}(D) \equiv \frac{A_{12}(D)}{A_{12}(D_{\text{ref}})}, \quad \eta_{\text{prob}}(D) \equiv \eta_{\text{amp}}(D)^2. \quad (\text{E12})$$

The reproducible script is `extract_eta_prefactor_1d.py` in the `code/` directory.

For non-fine levels in Table XX, we obtain

$$\max\left(\frac{|\eta_{\text{amp}} - \eta_{\text{amp}}^{(\text{fine})}|}{|\eta_{\text{amp}}^{(\text{fine})}|}\right) = 1.08 \times 10^{-2}, \quad \max\left(\frac{|\eta_{\text{prob}} - \eta_{\text{prob}}^{(\text{fine})}|}{|\eta_{\text{prob}}^{(\text{fine})}|}\right) = 2.18 \times 10^{-2}, \quad (\text{E13})$$

and the fine full-scan profile over $D = 4, \dots, 20$ gives $\eta_{\text{amp}} \in [0.9996, 1.1695]$ and $\eta_{\text{prob}} \in [0.9992, 1.3677]$ (source CSV: `output/eta_fp_1d/eta_prefactor_D4-5-...-20.csv`).

TABLE XX. 1D on-axis benchmark for η prefactor candidates at $D = \{6, 12, 18\}$ (coarse/mid/fine).
Source CSV: `output/eta_fp_1d/eta_prefactor_D6-12-18.csv`.

D	level	ΔE_{12}	S_1	A_{12}	η_{amp}	η_{prob}
6	coarse	2.6433×10^{-2}	4.28295	1.91521	1.04764	1.09755
6	mid	2.6475×10^{-2}	4.29274	1.93709	1.05923	1.12197
6	fine	2.6489×10^{-2}	4.28158	1.91661	1.04787	1.09803
12	coarse	3.6727×10^{-4}	8.51270	1.82812	1.00000	1.00000
12	mid	3.6889×10^{-4}	8.50865	1.82877	1.00000	1.00000
12	fine	3.6944×10^{-4}	8.50734	1.82906	1.00000	1.00000
18	coarse	5.2804×10^{-6}	12.75507	1.82864	1.00028	1.00056
18	mid	5.3189×10^{-6}	12.75845	1.84820	1.01063	1.02137
18	fine	5.3320×10^{-6}	12.74576	1.82936	1.00017	1.00033

TABLE XXI. Global-scan impact of η prefactor candidates (diagnostic only; not baseline).

case	$f(\mathcal{R}_3 > 0.90)$	$f(\mathcal{R}_3 > 0.95)$	$f(\chi^2_{\mu\mu} < 4)$	best χ^2
baseline $\eta_{\text{eff}} = \eta$	0.800	0.000	0.0942	3.05×10^{-7}
$\eta_{\text{eff}} = \eta \eta_{\text{amp}}(D)$	0.800	0.000	0.0939	9.66×10^{-7}
$\eta_{\text{eff}} = \eta \eta_{\text{prob}}(D)$	0.800	0.000	0.0942	2.00×10^{-6}
$\eta_{\text{eff}} = \eta_{\text{amp}}(D)$	0.800	0.000	0.1000	5.01×10^{-2}
$\eta_{\text{eff}} = \eta_{\text{prob}}(D)$	0.800	0.000	0.1000	4.85×10^{-2}

To quantify map-level sensitivity, we compare baseline $\eta_{\text{eff}} = \eta$ against profile-scaled and fully-closed variants on the same 60×60 grid. Results are summarized in Table XXI (source CSV: `paper/eta_profile_impact.csv`).

At current scan resolution, profile-scaled implementations are nearly degenerate with baseline map-level summaries, while fully closed $\eta_{\text{eff}} = \eta_{\text{fp}}(D)$ shifts proxy-fit quality more noticeably. Therefore, Eq. (E12) is reported as a first-principles candidate benchmark and is not propagated into baseline reported figures.

7. Action-Derived First-Principles Candidate for Superradiant Channel Scaling

To test a geometry-closed replacement direction for the channel normalization in Eq. (32), we keep the same 1D action-derived chain and define channel-resolved barrier actions

$$U_\ell(z; D) \equiv U(z; D) + \frac{\ell(\ell+1)}{z^2 + \varepsilon^2}, \quad S_{N,\ell}(D) \equiv \int_{z_-}^{z_+} dz \sqrt{U_\ell(z; D) - E_N(D)}, \quad (\text{E14})$$

TABLE XXII. 1D on-axis benchmark for superradiant profile candidates at $D = \{6, 12, 18\}$ (coarse/mid/fine). Source CSV: `output/superrad_fp_1d/superrad_prefactor_D6-12-18.csv`.

D	level	$\omega_{N_{\text{ref}}}$	$S_{N_{\text{ref}},1}$	$S_{N_{\text{ref}},2}$	\tilde{A}_1	\tilde{A}_2	$A_2^{(\text{fp})}/A_1^{(\text{fp})}$
6	coarse	0.738989	12.7478	20.7033	1.2936×10^4	5.5305×10^4	4.1247×10^{-7}
6	mid	0.739468	12.7644	20.7073	1.2452×10^4	5.4667×10^4	4.2192×10^{-7}
6	fine	0.739629	12.7711	20.7088	1.2652×10^4	5.6814×10^4	4.2589×10^{-7}
12	coarse	0.722035	17.5746	26.3029	1.0000	1.0000	9.6480×10^{-8}
12	mid	0.722513	17.5720	26.3009	1.0000	1.0000	9.6103×10^{-8}
12	fine	0.722674	17.5866	26.3217	1.0000	1.0000	9.4844×10^{-8}
18	coarse	0.719408	22.0000	31.0465	1.47×10^{-4}	7.9×10^{-5}	5.1810×10^{-8}
18	mid	0.719888	22.0060	31.0550	1.45×10^{-4}	7.8×10^{-5}	5.1411×10^{-8}
18	fine	0.720050	22.0043	31.0573	1.50×10^{-4}	8.0×10^{-5}	5.0954×10^{-8}

with $E_N = \omega_N^2 - m_0^2$ in bound-state convention. We then define geometry-driven channel rates

$$\Gamma_{N,\ell}^{(\text{geo})}(D) \equiv \omega_N(D) e^{-2S_{N,\ell}(D)}, \quad (\text{E15})$$

and infer effective channel normalizations by matching to Eq. (32):

$$A_\ell^{(\text{fp})}(D; N) \equiv \frac{\Gamma_{N,\ell}^{(\text{geo})}(D)}{\omega_N(D) (\omega_N(D) M_*)^{4\ell+4}}. \quad (\text{E16})$$

Using $(D_{\text{ref}}, N_{\text{ref}}) = (12, 2)$, we define profile factors

$$\tilde{A}_\ell(D) \equiv \frac{A_\ell^{(\text{fp})}(D; N_{\text{ref}})}{A_\ell^{(\text{fp})}(D_{\text{ref}}; N_{\text{ref}})}. \quad (\text{E17})$$

The reproducible script is `extract_superrad_prefactor_1d.py` in the `code/` directory.

For non-fine rows in Table XXII, the maximum relative deviations are

$$\max \left(\frac{|\tilde{A}_1 - \tilde{A}_1^{(\text{fine})}|}{|\tilde{A}_1^{(\text{fine})}|} \right) = 3.22 \times 10^{-2}, \quad \max \left(\frac{|\tilde{A}_2 - \tilde{A}_2^{(\text{fine})}|}{|\tilde{A}_2^{(\text{fine})}|} \right) = 3.78 \times 10^{-2}. \quad (\text{E18})$$

The fine full-scan profile over $D = 4, \dots, 20$ yields $\tilde{A}_1 \in [8.54 \times 10^{-6}, 4.10 \times 10^5]$ and $\tilde{A}_2 \in [3.95 \times 10^{-6}, 4.92 \times 10^6]$ (source files in `output/superrad_fp_1d/`), indicating a very stiff D -dependence in this preliminary closure.

To quantify map-level sensitivity, we compare baseline $(A_1, A_2) = (1, 1)$ against profile-scaled implementations on the same 60×60 grid. Results are summarized in Table XXIII (source CSV: `paper/superrad_profile_impact.csv`).

At current scan resolution, the action-derived superradiant profile candidate induces non-negligible shifts in both \mathcal{R}_3 coverage and proxy-compatibility area. Therefore, Eq. (E17) is reported as a first-principles diagnostic benchmark and is not propagated into baseline reported figures.

TABLE XXIII. Global-scan impact of superradiant profile candidates (diagnostic only; not baseline).

case	$f(\mathcal{R}_3 > 0.90)$	$f(\mathcal{R}_3 > 0.95)$	$f(\chi^2_{\mu\mu} < 4)$	best χ^2
baseline (A_1, A_2) = (1, 1)	0.800	0.000	0.0942	3.05×10^{-7}
$(A_1, A_2) = (\tilde{A}_1, \tilde{A}_2)$	0.7317	0.000	0.0358	2.23×10^{-4}
$(A_1, A_2) = 0.5(\tilde{A}_1, \tilde{A}_2)$	0.7106	0.000	0.0358	2.23×10^{-4}
$(A_1, A_2) = 2(\tilde{A}_1, \tilde{A}_2)$	0.7550	0.000	0.0358	2.23×10^{-4}

Appendix F: Ansatz Ablation Study

To demonstrate that the three-generation structure is robust and not an artifact of a particular ansatz choice, we compare the baseline Yukawa-proportional B_N (this work) against the alternative “inverse Yukawa” ansatz explored in earlier versions.

1. Inverse Yukawa Ansatz (Ablation A)

The inverse Yukawa ansatz sets $B_N^{(\text{inv})} \propto 1 / \sum_{f \in \text{Gen } N} y_f$, yielding:

$$B_1^{(\text{inv})} \approx 10^5, \quad B_2^{(\text{inv})} \approx 125, \quad B_3^{(\text{inv})} = 1. \quad (\text{F1})$$

This massive hierarchy ($B_1 \gg B_2 \gg B_3$) directly encodes the answer by over-enhancing layer 1. While it can produce $\mathcal{R}_3 > 95\%$, the mechanism is less transparent: the visibility factor, rather than the entropic/kinetic competition, drives the result.

2. Comparison

- **Baseline (Yukawa-proportional):** $B_1 < B_2 < B_3$. The three-generation structure emerges from the $g_N - \Gamma_N$ competition modulated by modest B_N differences.
- **Ablation A (Inverse Yukawa):** $B_1 \gg B_2 \gg B_3$. Layer 1 is artificially boosted; the selection mechanism is less falsifiable.

We recommend the baseline as the primary closure due to its greater transparency and falsifiability.

[1] N. Gresnigt, Electroweak structure and three fermion generations in clifford algebra with s_3 family symmetry (2026), arXiv:2601.07857 [hep-ph].

- [2] A. Dabholkar, S. Murthy, and D. Zagier, Quantum black holes, wall crossing, and mock modular forms (2012), arXiv:1208.4074 [hep-th].
- [3] J. Maldacena and L. Susskind, Fortschritte der Physik **61**, 781 (2013), arXiv:1306.0533 [hep-th].
- [4] J. L. Cardy, Nucl. Phys. B **270**, 186 (1986).
- [5] J. D. Bekenstein, Phys. Rev. D **7**, 2333 (1973).
- [6] G. 't Hooft, Dimensional reduction in quantum gravity (1993), arXiv:gr-qc/9310026 [gr-qc].
- [7] S. Detweiler, Phys. Rev. D **22**, 2323 (1980).
- [8] S. Navas *et al.*, Phys. Rev. D **110**, 030001 (2024), particle Data Group.
- [9] ATLAS Collaboration, Phys. Rev. Lett. **135**, 231802 (2025), arXiv:2507.03595 [hep-ex].
- [10] V. Gorini, A. Kossakowski, and E. C. G. Sudarshan, J. Math. Phys. **17**, 821 (1976).
- [11] G. Lindblad, Commun. Math. Phys. **48**, 119 (1976).
- [12] J. C. F. Thaler and S. Trifinopoulos, Phys. Rev. D **111**, 056021 (2025), arXiv:2410.23343 [hep-ph].